FIBER OPTIC TEMPERATURE AND VIBRATION SENSORS

FIBER OPTIC TEMPERATURE AND VIBRATION SENSORS

A Thesis

Submitted to the School of Graduate Studies

In Partial Fulfilment of the Requirements

For the Degree

Master of Applied Science

McMaster University

Master of Applied Science (2008)		McMaster University
(Engineering Physics)		Hamilton, Ontario

TITLE: Theory and Experiments of Fiber Optic Temperature and Vibration Sensors
AUTHOR: Clyde Albert Jr. Barry Stoute, B. Eng. (Concordia University)
SUPERVISOR: Dr. Paul E. Jessop
NUMBER OF PAGES: 95

Abstract

Fiber optic temperature and vibration sensors were designed and built to take readings in the harsh environment of a steel mill. The sensors are insensitive to electromagnetic noise; making them well suited for the use in such an environment. The temperature sensor uses an optical filter technique. A piece of intrinsic silicon is inserted between two optical fibers and 1064nm wavelength light is transmitted through the silicon. As the temperature increases, the silicon becomes more highly absorbing. The vibration sensor uses an optomechanical technique. Light is transmitted across a short air gap between two optical fibers. One of the fibers acts as cantilever while the other is fixed. As the cantilever vibrates, the transmitted power fluctuates, which enables the detection of the frequency and amplitude of the vibration. Sensors were initially tested under laboratory conditions, and subsequently field tested at ArcelorMittal Dofasco. The temperature sensor has a sensitivity of 0.4^{0}C over the temperature range from 22^{0}C to 120^{0}C. The vibration sensor has a sensitivity of 2.87mV/g peak over a frequency range from 0 to 1250 Hz.

Acknowledgements

I like to thank my family: Clyde, Jocelyn, Karen and Shawn Stoute for the support. Also, I like to thank my supervisor, Dr. Paul E. Jessop.

Table of Contents

i. Table of Figures

1 Introduction

The aim of this research is to develop photonic temperature and vibration sensors for harsh environments. The motivation for the project came from ArcelorMittal Dofasco who sponsored the work in partnership with the Ontario Centre of Excellence (OCE). The company identified a specific requirement for sensors that can monitor the temperature and vibration of motors and bearings within a steel mill; however, the sensors that have been developed can also be used in a wide range of other environments and applications.

An essential feature of the photonic sensors is to have no electronic components at the site of the measurements. Thus, all the data collecting equipment must be in a remote control room so that it can be shielded from the harsh environment. The sensors must be compact (a few cubic centimetres) and must be interrogated via optical fiber. The application envisioned by ArcelorMittal Dofasco, requires a sensor that can read temperature within 5% of the actual temperature. As for the vibration, they anticipate acceleration measurements in the range between 0 to 2g's or $19.62 m/s^2$.

The temperature sensor is an extrinsic optical fiber sensor; this means the fiber is used to transmit light to and from a sensing medium, but the sensor itself is not the fiber. In this case, the medium for the sensor is undoped silicon. The band edge wavelength for any semiconductor is highly temperature dependent. The measurement of temperature is accomplished by measuring the relative transmission of light for a wavelength near the band edge. The vibration sensor is an intrinsic optical fiber sensor, meaning that the optical fiber is the actual sensor element. This is an optomechanical sensor in which the vibration is sensed by monitoring the overall power loss, which is dependent on the movement of a fiber optic cantilever beam.

An extensive literature search was conducted to determine what other groups have developed. Other researchers made alterations to the cantilever fiber, such as adding a seismic mass to the cantilever fiber. With regard to the temperature sensor literature review, the main purpose was to research how the band gap and the index of refraction change with temperature.

Although that the two sensors are fundamentally different in terms of their physical mechanisms, they have much in common in terms of assembly, packaging and instrumentation. Before packaging, the sensors underwent laboratory testing to make sure they performed as expected. When the sensors are packaged, they went through laboratory testing as well as industrial testing to determine their durability.

2 Background Theory

2.1 Temperature Dependence of Absorption Coefficient

Semiconductors are virtually opaque for photon energies greater than the bandgap energy and, if lightly doped, highly transparent for photon energies below the bandgap. The transition between opaque and transparent occurs smoothly over a narrow range of wavelengths that is centered at the bandgap wavelength. Since the bandgap changes with temperature, the semiconductors attenuation coefficient changes within this wavelength range. "The variation of the energy gap with temperature originates from two different processes[1]". The first process is the variation with bond length in relation to the temperature. This is linked to the pressure coefficient via compressibility and the thermal expansion coefficient. The second process is due to the electron-phonon interaction. The second process overtakes the first at temperatures higher than 100 Kelvin. The following four analytical equations will help to clarify our previous statements. The equations will be given and then explained in both their theoretical and application meaning. A graphical representation will then be given[1]:

$$E_g(T) = E_g(0) - \frac{\alpha_0 T^2}{T + \beta} \qquad (2.1)$$

$$E_g(T) = E_B - a_B \left[1 + \frac{2}{\exp(\theta / T) - 1} \right] \qquad (2.2)$$

$$E_g(T) = E_g(0) + BT + CT^2 \qquad (2.3)$$

$$E_g(T) = E_g(0) - \frac{\alpha\theta}{2} \left[\sqrt[p]{1 + \left(\frac{2T}{\theta} \right)^p} - 1 \right] \qquad (2.4)$$

$E_g(0)$: Initial Bandgap Energy at $22^0 C$ (eV)

α_0 : Fitting Parameter (eV/K)

β : Debye Temperature (K)

E_B : Bandgap energy in Bose - Einstein Model (eV)

a_B : Strength of the electron - phonon interaction (MeV)

θ : Temperature in Phonon Mode (K)

B : Fitting Parameter (eV/K)

C : Fitting Parameter (eV/K^2)

α : Fitting Parameter (eV/K)

The first equation was derived from Varshni and it is the most commonly used one in optical temperature sensing. The second equation, the most recent one, is the Bose-Einstein empirical expression in which the energy gap at 0 Kelvin is given by $E_g(T) = E_B - a_B$. The third and fourth equations were derived by O'Donnell & Chen and Pässler respectively. Both the effects of thermal expansion and electron-phonon interaction are not taken in account in all the equations. Thus, the parameters' physical meaning is not always obvious[1].

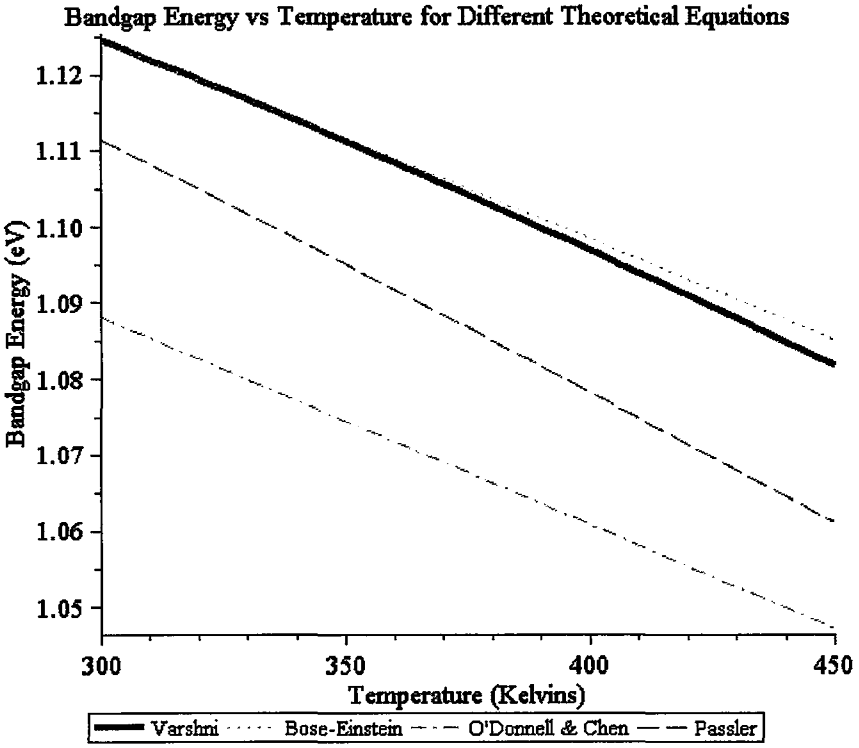

Figure 2.1.1: Bandgap Energy vs. Temperature for Different Theoretical Equations

Figure 2.1.1 shows the curves of different theoretical equations from 2.1, 2.2, 2.3 and 2.4 respectively. The bold curve represents the Varshni equation while the three dash lines represent the Bose-Einstein, O'Donnell & Chen and Pässler equations.

According to the many researchers who have done experiments with the photoluminescence or absorption measurements, many of the data points fit the Varshni equation in the range from 1.5^0K to 750^0K. Thus for this research, the Varshni equation of energy bandgap will be used to model the transmission[2].

The first parameter, $E_g(0)$, is the bandgap energy for silicon at 0 Kelvin. The second parameter, β, is the Debye Temperature. In brief, the Debye Temperature is the compensation for the contribution of phonons to the specific heat. The last parameter, α_0, is the fitting parameter of the Varshni equation[2].

For photon energies near the bandgap energy, the absorption coefficient (units in cm^{-1}) depends on photon energy as[3]:

$$\alpha = K\left[h\nu - E_g(T)\right]^P \quad (2.5)$$

K and P are the transition probability constant and the optical absorption process index respectively. Normally, K and P have the values of 2400 $cm^{-1}eV^{-P}$ and 1.5 respectively[3]. The P value is assumed to be correct; however the K value is subject to change depending on the nature of silicon (doping and defect levels) and external factors such as dust and dirt[3].

The main aspect of this research is developing a silicon filter to sense the temperature. The temperature will be detected and interpreted in terms of transmission of light[4]:

$$I = I_0 \exp(-\alpha L) \qquad (2.6)$$

Where L is the thickness of the sample in centimeters. With equation 2.1, 2.5 and 2.6, the relative transmission I/I_0, is therefore given by:

$$Transmission = \exp\left(-K\left[\frac{hc}{\lambda} - E_g(0) + \frac{\alpha_0 T^2}{T+\beta}\right]^{1.5} \cdot L\right) \qquad (2.7)$$

With these equations, we can plot the transmission in relation to temperature at different thickness using the following parameters: K = 2400 $cm^{-1}eV^{-1.5}$, h = 4.13566733×10^{-15}eV·s, $E_g(0)$ = 1.17eV, c = 2.998×10^{8}m/s, λ = 1064×10^{-9}m, α_0 = 473×10^{-6} eV/K, β = 636 K, the curves look like the following with the L ranging from 100μm to 500μm[5, 6].

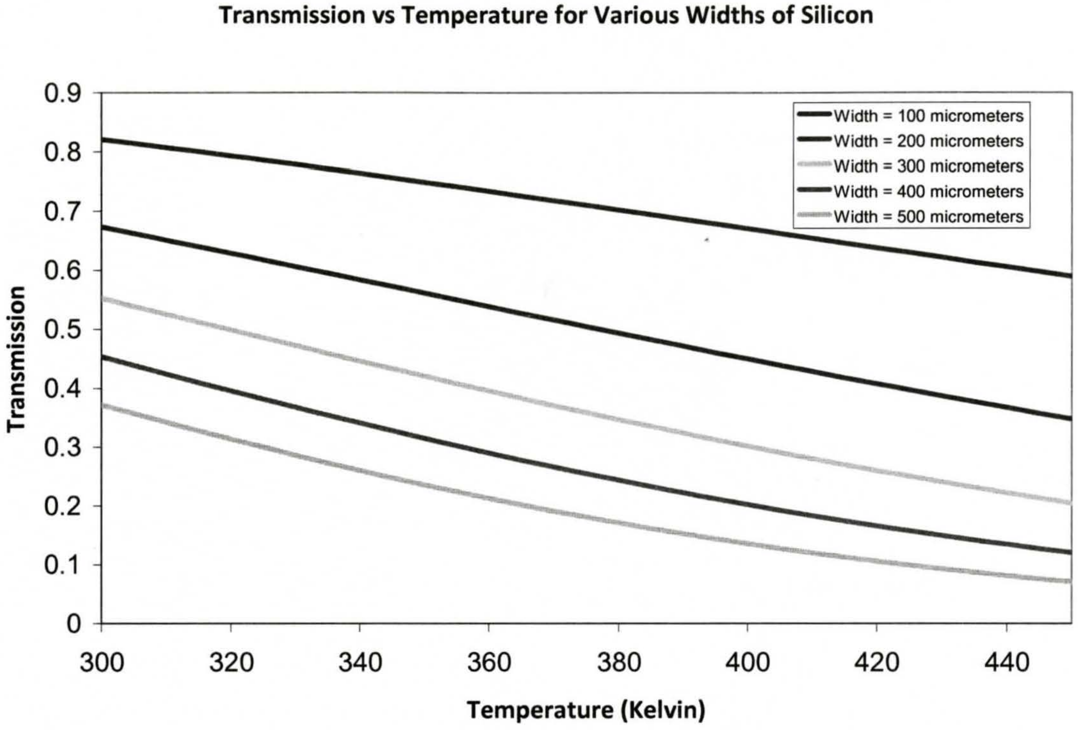

Figure 2.1.2: Transmission vs. Temperature at Various Thickness of Silicon for $\lambda=1064nm$

2.2 Mechanics

The fiber optic vibration sensor is based on monitoring the variations in the power coupled between two fibers separated by a short air gap, with one fiber suspended as a cantilevered beam. Therefore we need to examine the basic mechanics of a cantilever system to estimate the sensitivity and frequency response of the sensor.

2.2.1 Modeling Physical Systems

The description of a mechanical system involves six degrees of freedom, which are characterised by the variables {X, Y, Z} and {Φ, Θ, Ψ}. The {X, Y, Z} represents the linear motion in the (i, j, k) directions while {Φ, Θ, Ψ} represents the rotation about the (i, j, k) directions. Before modeling the system, one must understand the dynamics of rigid body as described by Coriolis' equation of motion[7]:

$$\frac{d\vec{r}}{dt}|_I = \frac{d\vec{r}}{dt}|_B + \vec{\omega} \times \vec{r} \qquad (2.8)$$

In equation 2.8, variables $\vec{r}$ and $\vec{\omega}$ are the position and angular velocity of the body respectively. I and B are the inertial frame and body frame respectively. The vector $\vec{r}$ can be represented in Cartesian coordinates (x, y, z) or in cylindrical coordinates (r, θ, z). This implies that the rate of change of position in the inertial frame (a frame that is fixed and cannot be moved) is the rate of change of position in the body frame (a frame that can be translate and rotate with respect to the fixed frame) plus the cross product of the angular velocity and the position. This simple equation allows the derivation of the velocity and the acceleration in full. For simplicity, we will look at the acceleration of the system only given as[7]:

$$\vec{a} = \ddot{\vec{r}} + \dot{\vec{\omega}} \times \vec{r} + 2\vec{\omega} \times \dot{\vec{r}} + \vec{\omega} \times \vec{\omega} \times \vec{r} \quad (2.9)$$

The acceleration equation contains four terms: radial acceleration ($\ddot{\vec{r}}$), the tangential acceleration ($\dot{\vec{\omega}} \times \vec{r}$), the Coriolis acceleration ($2\vec{\omega} \times \dot{\vec{r}}$) and the normal acceleration ($\vec{\omega} \times \vec{\omega} \times \vec{r}$)[1]. Notice the total acceleration equation is not a single term; it is a combination of four different acceleration terms. However, the only acceleration that is necessary is the normal acceleration. The reason is that the majority of motor assemblies are not balanced; thus there is an eccentric load. The motors tend to rotate at constant angular velocity thus tangential acceleration is non-existent. Coriolis and radial acceleration are not available because there is no change in the radius of the eccentric load. Therefore, normal acceleration is the only major acceleration causing vibration in the motor.

2.2.2 Solid Mechanics

Every mechanical system has three main components: mass, spring and a damper. For this research and application, we are primarily concern with the mechanical vibration of a cantilever beam application. To find the mechanical vibration sequence of the cantilever beam, our analysis will use solid mechanics[8]. The following force distribution figure shows the relations of distributed forces on a beam and the resultant changes.

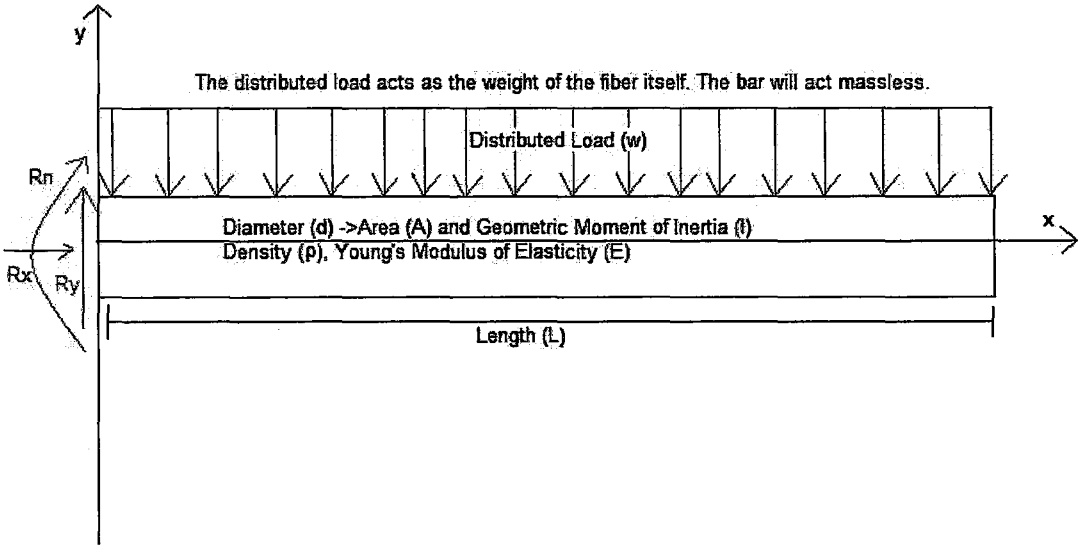

Figure 2.2.2.1: Cantilever Beam Analysis

Figure 2.2.2.1 shows the analysis of the cantilever beam. The R_N represents the reaction moment in the $\hat{k}$ - axis. This moment only appears in the fixed structures, such as cantilever beams. The R_X and R_Y are the reaction forces in the $\hat{i}$ - and $\hat{j}$ - axis. Reaction forces and moments are there to balance the external forces exerted on the structure. These will appear in any hinges or pinned-wheels; in this case, these reactions all occur at one spot, the fixed end of the cantilever. The other end of the cantilever is completely free. Reaction forces and moments are in units of Newtons (N) and Newton-meters (N·m). To have a better understanding of the solid mechanics analysis, we can assume that the beam is massless with distributed load along its length. The distributed load compensates for the weight of the beam. The units of the distributed load are in Newtons per meter (N/m)[8].

Young's Modulus of Elasticity (E) determines the stiffness of the material. It is dependent on the stress related to the strain of the material. The common units of elasticity are given in gigapascals (GPa)[8].

Inertia (I) is the amount of resistance to the motion of a structure. The larger the moment of inertia, the more resistant to motion it is. There are two types of inertia, mass and geometric. Mass moment of inertia applies to objects in motion and has its units in kilograms meters square ($kg \cdot m^2$). However, mass moment of inertia is not a concern in this research. Geometric moment of inertia (also known as the second moment of area) applies to change in the structural shape of the object and has the units of meters to the fourth power (m^4)[8].

With these parameters, we use the beam deflection differential equation to derive the deflection equation:

$$EI\frac{\partial^4 y(x,t)}{\partial x^4} + \rho A\frac{\partial^2 y(x,t)}{\partial t^2} = 0 \qquad (2.10)$$

To simplification the equation, the time component of the equation will be ignored.

First, we have to develop the boundary conditions for the cantilever beam[8,9]:

$$\left. y(x,t) \right|_{x=0} = 0 \qquad (2.11.i) \qquad \left. \frac{\partial}{\partial x} y(x,t) \right|_{x=0} = 0 \qquad (2.11.ii)$$

$$\left. \frac{\partial^2}{\partial x^2} y(x,t) \right|_{x=L} = 0 \qquad (2.11.iii) \qquad \left. \frac{\partial^3}{\partial x^3} y(x,t) \right|_{x=L} = 0 \qquad (2.11.iv)$$

From equation 2.10 without the time component, and using the boundary conditions of group 2.11, we will form our cantilever beam equation. The beam equation is the initial step in for the development of the natural frequency equation. For simplicity, we will use the final equation[10].

$$EIy(x) = -\frac{wx^4}{24} + \frac{wLx^3}{6} - \frac{wL^2x^2}{4} \qquad (2.12)$$

2.2.3 Mechanical Vibration

From the preceding results, we can derive the cantilever beam deflection equation and proceed towards finding the mechanical vibration of the cantilever beam. There is no direct way to find the natural frequency of the beam via this equation alone; however we can find the stiffness of the cantilever. Since time is not a factor in the cantilever beam analysis, the following equations has been simplified as follows[11]:

Derivation of the Natural/Resonance Frequency Equation

$$w = \rho \cdot A \cdot a \tag{2.13}$$

$$m = \rho \cdot A \cdot L \tag{2.14}$$

$$x = L \tag{2.15}$$

$$EIy(L) = EI\delta = -\frac{\rho AaL^4}{24} + \frac{\rho AaL^4}{6} - \frac{\rho AaL^4}{4} \tag{2.16}$$

$$\delta = -\frac{\rho AaL^4}{8EI} \tag{2.17}$$

$$F = \rho ALa = k \cdot \delta \rightarrow k = \frac{F}{\delta} \tag{2.18}$$

$$k = \frac{8EI}{L^3} \tag{2.19}$$

$$\omega_n = 2\pi f_n = \sqrt{\frac{k}{m}} \tag{2.20}$$

$$f_n = \frac{1}{2\pi}\sqrt{\frac{8EI}{\rho AL^4}} \tag{2.21}$$

w : *Distributed Load (N/m)*
m : *Mass (kg)*
ρ : *Density (kg/m^3)*
a : *Acceleration (m/s^2)*
L : *Length of the beam (m)*
A : *Cross - section Area (m^2)*
x : *Linear position of the beam (m)*

E: Modulus of Elasticity (Pa)
I: Geometric Moment of Inertia (m^4)
δ : Deflection of the beam (m)
F : Force (N)
k : Stiffness constant (N/m)
ω_n : Resonance Frequency (rad/s)
f_n : Resonance Frequency (Hz)

To begin, we start by writing down the distributed load, mass and position relations respectively (2.13-15). Then we use the deflection equation that was developed from equation 2.12 and replaced w, m and x to form equation 2.16. That resultant equation is the deflection constant at the end of the cantilever; thus, we can replace y(L) with δ to represent deflection constant, which leads to equation 2.17. In equation 2.18, we rewrote the force equation to represent the weight of the beam; then we equated it to Hooke's Law; thus finding the stiffness (or spring) constant of the cantilever shown in 2.19. We know that the natural frequency is the square root of the stiffness divide by the mass (2.20). Replace k and m into the natural frequency equation and the result will be the natural frequency equation as shown in 2.21. In Chapter 4 Design section, we will look at how the length, the area and the geometric inertia influence the natural frequency of the fiber.

The natural frequency dictates that at a certain frequency, the body will be resonating. At resonance, all readings will be inaccurate and imprecise up to two and a half times the natural frequency. At this point, the device will act as a seismometer instead of an accelerometer. The difference between the two is a seismometer is a device that measures the position of an object; an accelerometer is a device that measures the acceleration of an object[11].

Now, that the natural frequency has been found, we can use it to develop the motion equation of the sensor[11,12]:

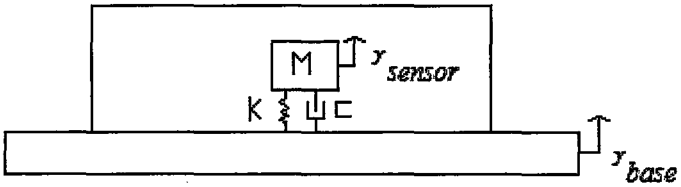

Figure 2.2.3.1: Free-Body Diagram of the Sensor

$$m\ddot{y}_{sensor} + c\left(\dot{y}_{sensor} - \dot{y}_{base}\right) + k\left(y_{sensor} - y_{base}\right) = 0 \qquad (2.22.i)$$

$$\text{Let } s = y_{sensor} - y_{base} \qquad (2.22.ii)$$

$$m\ddot{s} + c\dot{s} + ks = -m\ddot{y}_{base} \qquad (2.22.iii)$$

$$s(t) = Se^{-\zeta\omega_n t}\left(\cos\left(\omega_d t\right) + \cos\left(\omega_d t\right)\right) + \frac{Y_{base} \cdot r^2}{\sqrt{\left(1-r^2\right)^2 + \left(2\zeta r\right)^2}}\cos\left(2\pi ft - \arctan\left(\frac{2\zeta r}{1-r^2}\right)\right) \qquad (2.22.iv)$$

$$\text{Such that } s(t) = y_{sensor}(t) - y_{base}(t),\ r = \frac{f}{f_n},\ \zeta = \frac{c}{c_c} \text{ and } \omega_d = \sqrt{1-\zeta^2}\,\omega_n$$

We start with a simple modeling analysis of the system. Despite that we have a cantilever beam sensor, we can approximate it to a simple mass-spring-damper system. We fit two frames in the system: one at the mass (y_{sensor}) and one at the base (y_{base}). Now, we create the differential equation of the system. In equation 2.22.ii, that statement allows to measure the relative position of the sensor. After the replacement, in equation 2.22.iii, the input function is the base, which is the motor itself. We solve equation 2.22.iii to get the time domain of the system (2.22.iv). There are several components that appear in the equation. There is the time component, t. The natural damped frequency, ω_d, is when the structure is left alone after an initial shock, the structure vibrates at a certain frequency, the damped frequency, until the structure comes back to rest. The frequency ratio, r, is the input frequency over the natural frequency of the system. Lastly, the damping ratio, ζ, is the ratio of the damping coefficient (c) over the critical damping constant (c_c). The critical damping constant is $2(km)^{1/2}$. We can analyze the magnitude and phase versus the frequency ratio and the damping ratio. Below are the two plots of the magnitude and phase of the equation above[12]:

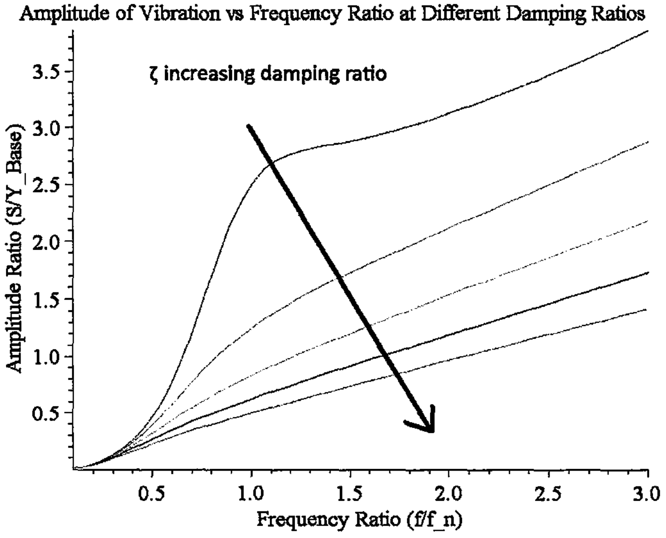

Figure 2.2.3.2: Amplitude Ratio vs. Frequency Ratio vs. Damping Ratio using Maple 11

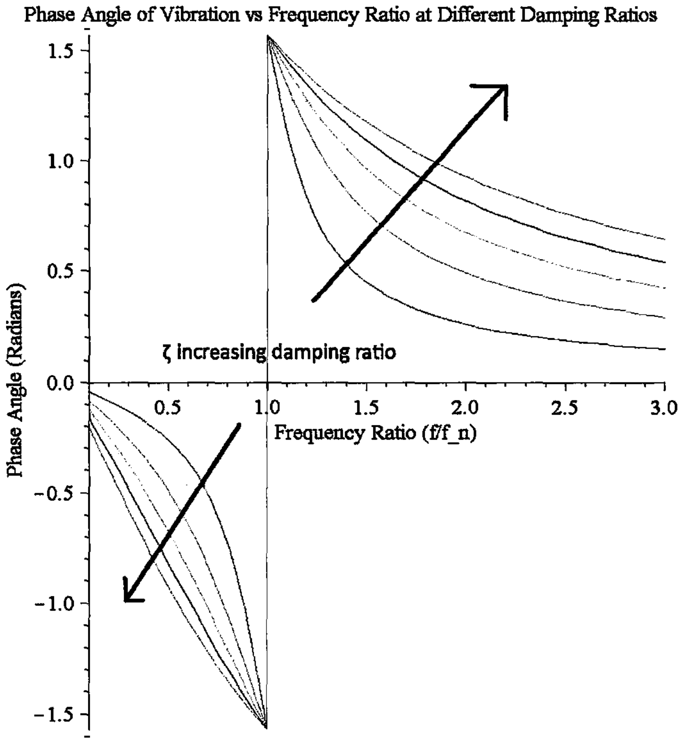

Figure 2.2.3.3: Phase Angle vs. Frequency Ratio vs. Damping Ratio using Maple 11

In order to have a useful accelerometer, the frequency ratio, r, has to be less than 0.25[11].

Using the combined knowledge of solid mechanics and mechanical vibration, we can then proceed to apply this knowledge to optical systems. Later on, there will be further discussion on the design of the cantilever beam and the results of the vibration sensors built and tested.

2.3 Lightwave Propagation

In this section, we will describe the elements of electromagnetic theory that relate to light wave propagation in free space and optical fibers, as required for an understanding of the fiber optic sensors that were developed.

2.3.1 Optical Fiber Modes

An electromagnetic wave consists of coupled electric and magnetic waves propagating through a medium perpendicular to each other, and in phase with each other[13]. Electromagnetic radiation has dual properties: wave and particle. The wave model describes the propagation of coupled electric and magnetic waves with velocity[14]:

$v = f\lambda$ *where f is the frequency in* sec^{-1} *and* λ *is the wavelength in meters (2.23.i)*

In a vacuum, the velocity of the wave is the speed of light, c; in any other medium, the velocity of the wave is reduced as per to the equation[15]:

$v = cn^{-1}$ *where n is the index of refraction of the medium (2.23.ii)*

The particle model of light quantizes the energy in the wave into a discrete packet. According to Planck's equation, the frequency and the energy are directly proportional[16]:

$$E = hf \qquad (2.23.iii)$$

The coefficient 'h' is Planck's constant, given as $6.62608696*10^{-34}$ Js[17].

Electromagnetism is governed by Maxwell's equations. These equations show the interrelationship between electric and magnetic fields, electric charge and current. Maxwell's equations are shown as following[17]:

$\nabla \bullet \vec{B} = 0$ (2.24 and 2.25) $\nabla \bullet \vec{D} = \rho$	$\nabla \times \vec{E} = -\frac{\partial \vec{B}}{\partial t}$ (2.26 and 2.27) $\nabla \times \vec{H} = \vec{J} + \frac{\partial \vec{D}}{\partial t}$
ρ = Charge Density $\vec{E}$ = Electric Field $\vec{D}$ = Electric Displacement Field	$\vec{J}$ = Current Density $\vec{H}$ = Magnetic Field Strength $\vec{B}$ = Magnetic Field $\vec{M}$ = Magentization $\vec{p}$ = Electric Dipole Moment per volume μ = Permeability ε_0 = Permittivity of free space μ_0 = Permeability of free space
$\vec{D} = \varepsilon_0 \vec{E} + \vec{p}$ $\vec{B} = \mu_0 (\vec{H} + \vec{M})$	

If we assume the light is passing through a linear, isotropic and uniform medium and that the electric charge density is zero, the electric dipole moment is directly proportional to the electric field[17]:

$\vec{p} = \varepsilon_0 \chi \vec{E}$ such that χ is the susceptibility (2.28)

$\vec{\mathrm{D}} = \varepsilon_0 \vec{E}(1+\chi) = \varepsilon_0 \varepsilon_r \vec{E} = \varepsilon \vec{E}$ (2.29)

The ε represents the permittivity of the material. With the assumptions, which are valid for lightwave propagation in optical fibers, Maxwell's Equation simplifies as follows[18]:

$\nabla \bullet \vec{E} = 0$ (2.30 and 2.31) $\nabla \bullet \vec{H} = 0$	$\nabla \times \vec{E} = -\mu \frac{\partial \vec{H}}{\partial t}$ (2.32 and 2.33) $\nabla \times \vec{H} = \varepsilon \frac{\partial \vec{E}}{\partial t}$

The solution for the EM waves for light is in the form of the following, in cylindrical coordinates:

$$\vec{\mathrm{E}}(\mathrm{r}, \varphi, \mathrm{z}, \mathrm{t}) = \vec{\mathrm{E}}_0(\vec{s}, t) \cdot \exp\left(i(\vec{k} \bullet \vec{s} - \omega t)\right) \qquad \text{such that } s = (r, \varphi, z) \quad (2.34)$$

The k is the wavenumber and it equals to $2\pi/\lambda$ and its units are in m^{-1}. The wavenumber is the magnitude of the wave vector[18].

In any optical fibers, the fiber modes within the core are in a shape of the Bessel function. The Bessel beam is a non-diffractive beam that propagates through the optical fiber. The Bessel beam function is shown in the following equation[19]:

$$E(r, \phi, z, t) = E_0 \exp\left(i\left(-\omega t + k_{\parallel} z\right)\right) \cdot J_0\left(k_{\perp} r\right) \qquad (2.35)$$

$$\text{Where } k_{\parallel} = \frac{2\pi}{\lambda}\cos(\theta), k_{\perp} = \frac{2\pi}{\lambda}\sin(\theta)$$

J_0 is the Bessel function of the zeroth order

Within the optical fiber, the fundamental mode of light is show below:

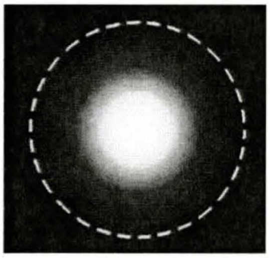

Figure 2.3.2.1: The fundamental mode of light in an optical fiber [20].

2.3.2 Free Space Propagation

Once the light leaves the optical fiber, we can approximate the mode shape as a Gaussian function. The Gaussian beam is a solution of the Helmholtz equation. The solution of the mathematical equation is in complex amplitude of the electric field. Below are the equations of the Gaussian beam[21]:

$$I(r,z)=I_0\left(\frac{w_0}{w(z)}\right)^2 \exp\left(\frac{-2r^2}{w^2(z)}\right) \qquad (2.36)$$

$$R(z)=z\left(1+\left(\frac{z}{z_0}\right)^2\right) \qquad (2.37)$$

$$w(z)=w_0\sqrt{1+\left(\frac{z}{z_0}\right)^2} \qquad (2.38)$$

$$z_0=\frac{\pi w_0^2}{\lambda} \qquad (2.39)$$

Each equation will be explained in detail in ascending order. The $z_0=\frac{\pi w_0^2}{\lambda}$ is the Rayleigh's length. Note that w_0 is the waist size of the beam. Rayleigh's length is the "distance from the beam waist to where the mode area is doubled."[19] The purpose of the Rayleigh's length is to determine the focus depth. Thus, there is a trade-off; the shorter the Rayleigh's length, the higher the optical intensity in its focus and stronger the focus of the beam. w(z) is the spot size of the beam. Above shows that w(z) is related to the axial distance z along the beam. R(z) is the radius of curvature of the wavefronts within the beam. At the end of the Gaussian beam equation, there is the parameter called the Guoy phase. The arc tangent of the axial distance to the Rayleigh's length (arctan[z/z_0]); the Guoy phase is the longitudinal phase delay of the beam[21].

With the vibration and temperature sensors, there are physical gaps between the two fibers, whether it is air, epoxy or silicon; having these gaps will cause the light to diverge. The laser beam diverges very quickly once it escapes from the fiber. Looking at the parameter w(z), if $z \gg z_0$, there will be an angle between the straight line and the center axis of the beam. This is called the divergence of the beam and the equation is given below[22]:

$$\theta \approx \frac{\lambda}{\pi w_0};\Theta = 2\theta \qquad (2.40)$$

θ and Θ are the beam divergence and the total angular spread of the beam (both in mrad) respectively[22, 23].

2.3.3 Fiber-to-Fiber Coupling

Fiber-to-Fiber Coupling is important in understanding the vibration sensor as well as the temperature sensor. The two main issues in the coupling are the lateral and longitudinal separation of the fibers and the angle mismatch. In this work, we are concerned with the coupling between two single-mode fibers separated by a small gap. The longitudinal separation needs to be analyzed for both the temperature and vibration sensors, keeping in mind that the temperature sensor has a silicon barrier that reduces the transmission significantly. The lateral separation and the angle mismatch only apply to the vibration sensor. This analysis is based on a generic optical fiber from Optics for Research[24].

Longitudinal separation has minimum sensitive to fiber coupling. The coupling power, unit-less, due to longitudinal displacement is described in the following equations[24]:

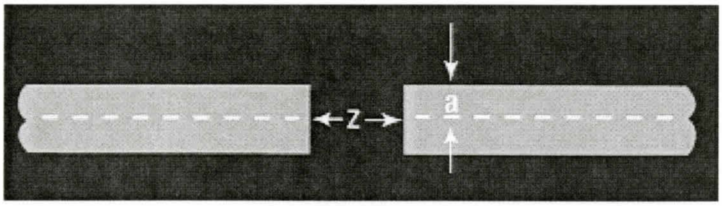

Figure 2.3.3.1: Longitudinal Displacement of Two Fibers[24]

$$CouplingPower = \left(\frac{1}{Z^2+1}\right); \qquad Z = \frac{z \cdot \lambda}{2\pi \cdot n_0 \omega_0^2} \qquad (2.41)^{24}$$

Note that λ, n_0 and ω_0 are the wavelength of the light, the index refraction of the gap (whether it is air or silicon), and the mode field radius along the beam axis (3.1µm for 1064nm wavelength) respectively[23]. The mode field radius is the width of the Bessel beam at the point where the intensity has decreased to $1/e^2$ of its maximum value. We can plot both the temperature sensor and the vibration sensor fibers as if both are facing each other[24].

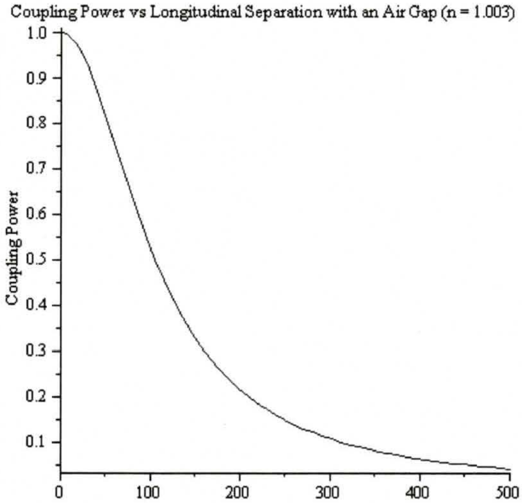

Figure 2.3.3.2: Coupling Power vs. Longitudinal Separation with an Air Gap

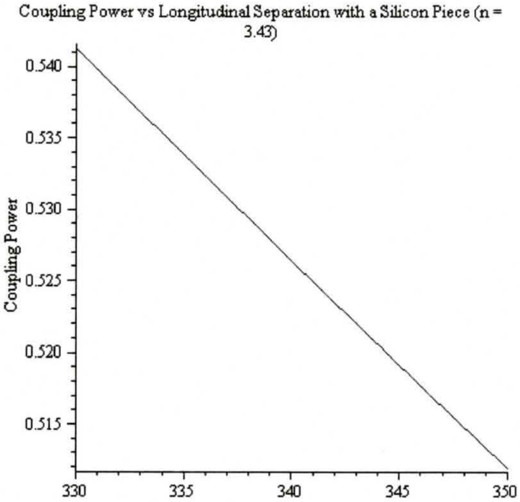

Figure 2.3.3.3: Coupling Power vs. Longitudinal Separation with a Silicon Piece

The lateral displacement is also important for the vibration sensor so that we can determine how much coupling power is available due to this offset. The coupling power due to the lateral offset shown in the figure below, is satisfied by the following equation:

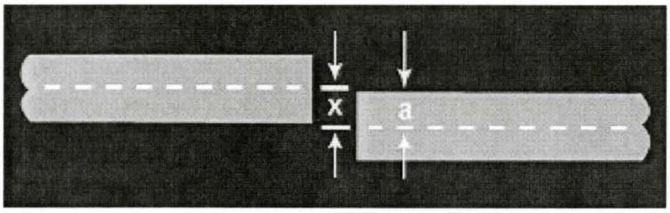

Figure 2.3.3.4: Lateral Displacement of Two Fibers[24]

$$CouplingPower = \exp\left(-\frac{x}{\omega_0}\right)^2 \qquad (2.42)^{24}$$

Below is the graph of the coupling power versus lateral displacement[24].

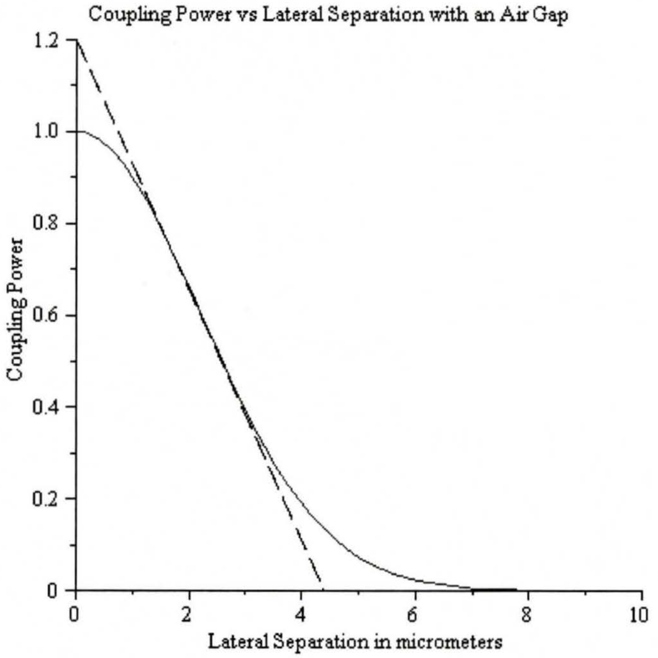

Figure 2.3.3.5: Coupling Power vs. Lateral Displacement with an Air Gap. The black dash line represents the slope at 2.5μm. The equation of the slope is y = 1.2 – 0.2715x. Thus the slope is 27.15% per μm.

Finally, the angular mismatch is another factor to consider in the vibration sensor. The function of the angular misalignment coupling power:

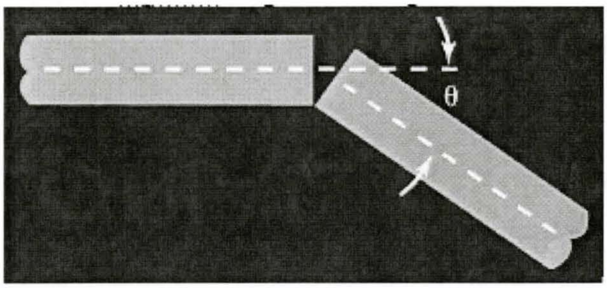

Figure 2.3.3.6: Angular Misalignment of Two Fibers[24]

$$CouplingPower = \exp\left(-\left(\frac{n_0 \pi \omega_0}{\lambda}\sin(\theta)\right)^2\right) \qquad (2.43)^{24}$$

The main factor is the angle which the misalignment makes with the beam axis. The equation is heavily dependent of this angle. Below is the graph of the coupling power due to the angle mismatch[24].

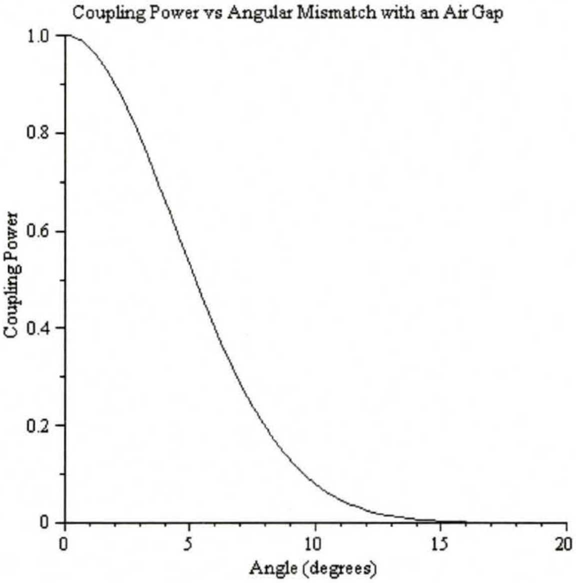

Figure 2.3.3.7: Coupling Power vs. Angle Mismatch with an Air Gap

The vibration sensor undergoes all three of these changes at the same time. Thus, there is a net coupling power between the offsets (both lateral and longitudinal) as well as the edge coupling power loss due to the angle change. All changes can be calculated via Monte Carlo analysis. This analysis allows all the parameters to "vary randomly to determine the statistical chance of a failure for a given set of tolerances.[25]" However, the loss is so small, it becomes negligible. Then, the Monte Carlo analysis of the coupling power within that range is linear[24].

2.3.4 Fabry-Pérot Effects

Another effect that takes place is the Fabry-Pérot effect. This effect can be described as when the incidental light goes from one medium to another, there is reflection and transmission. The Fabry-Pérot effect can be described in the following equations[26]:

$$T_e = \frac{1}{1 + F\sin^2(\delta/2)} \qquad (2.44)$$

$$F = \frac{4R}{(1-R)^2} \qquad (2.45)$$

$$\delta = 2nlk\cos\theta \qquad (2.46)$$

The T_e parameter represents the transmittance function; the F is the coefficient of finesse; while R is the reflection coefficient via Fresnel equations. The variables l, θ, n, and k are the thickness of the medium, the angle of incidence, the refractive index and the wavenumber respectively. Fresnel equations describe the interaction of light moving from one medium to another at different refractive indices. The equations are heavily dependent on the angle of incidence, θ[26]. However, since the research is based on a Gaussian beam approximation, the Fresnel equation for the reflection coefficient is governed by the following equation[27]:

$$R = \left(\frac{n_1 - n_2}{n_1 + n_2} \right)^2 \qquad (2.47)$$

Parameters n_1 and n_2 are the input and output mediums' refractive indices respectively. For observation of the light transmission, there were two different calculations: transmission vs. wavelength and transmission vs. length of the medium.

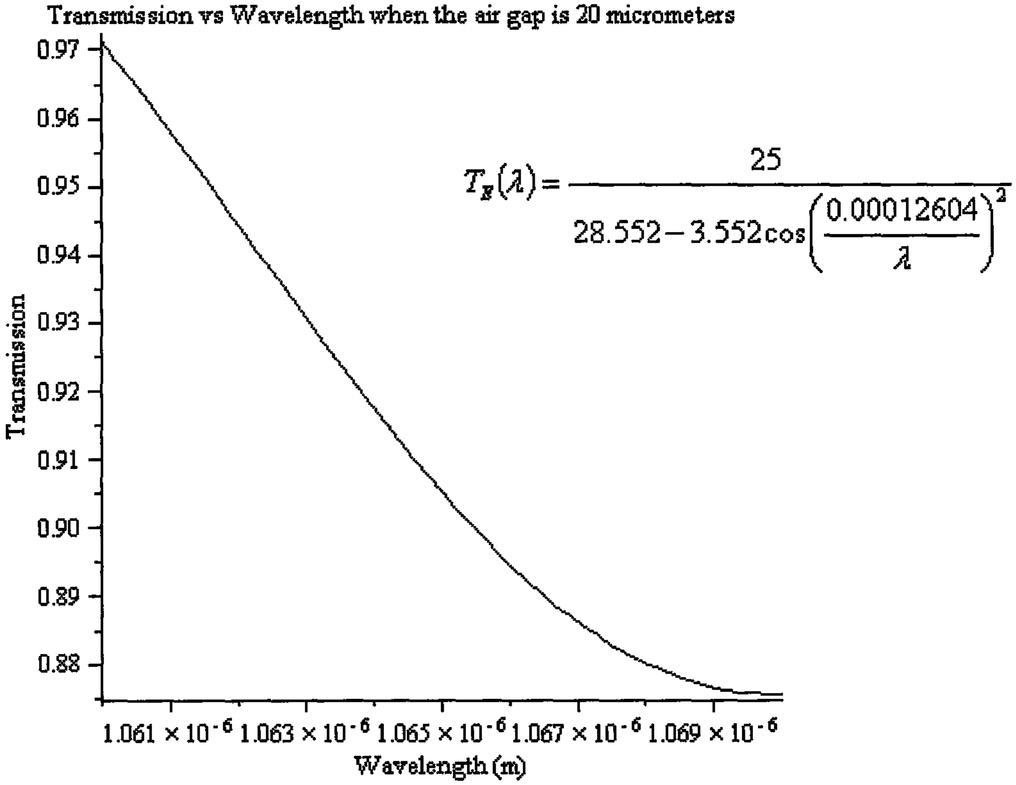

Figure 2.3.4.1: Transmission vs. Wavelength for an air gap of 20 micrometers. $T_E(\lambda)$ is the F-P equation in which the width of the medium is constant, wavelength varies.

This curve is approximately linear between 1060nm and 1065nm. Variation of wavelength changes the transmission by about 10% within the spectrum. Variation a 97% transmission level to an 87% transmission level can cause back reflection to the laser or scattering, which can cause a minute amount of cladding modes. Despite these claims, the variation in wavelength is so small, that the effects of these variations can be ignored.

Looking at the transmission vs. length of the air gap, there are some more significant issues to be dealt with:

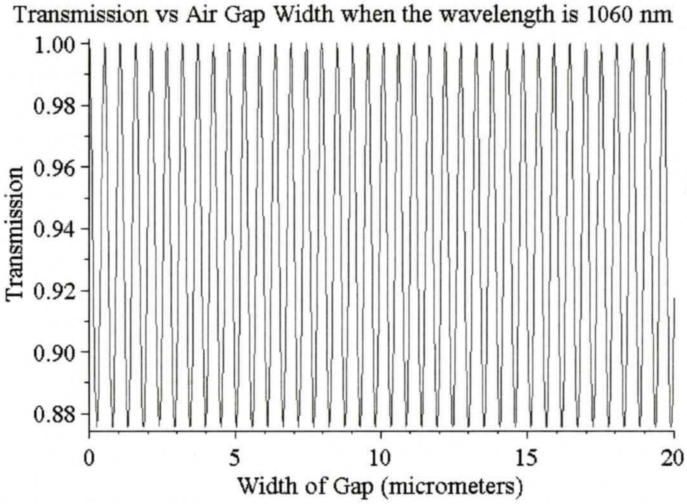

$$T_E(l) = \frac{25}{28.552 - 3.552\cos(5.923\cdot 10^{6} l)^{2}}$$

Figure 2.3.4.2: Transmission vs. Air Gap Width when the wavelength is 1060nm. $T_E(l)$ is the F-P equation in which the wavelength of the light is constant, width of the medium varies.

With these conditions, the width of the air gap is extremely sensitive. If the width is slightly off, the entire transmission can change. Thus, knowing precisely the distance between the two fibers is crucial [26, 27].

There is another equation that needs to be examined to observe the relation between the fringes and temperature. Observing the optical path difference at normal incidence, we can predict the number of fringes that appears when there is a change of temperature[28]:

$$\Gamma = 2nl \qquad (2.48)$$

With the normal incidence of light, the only concern is the maxima in transmission of light; thus, Γ will equal to mλ such that m is an integer from one to infinity. Rearranging the value to isolate m, the fringe equation is[29]:

$$m = \frac{2nl}{\lambda} \qquad (2.49)$$

Taking the derivative of equation 2.48 in terms of temperature:

$$\frac{dm}{dT} = \frac{2l}{\lambda} \cdot \frac{dn}{dT} \qquad (2.50)$$

This equation determines how many fringes there are per degree Celsius or Kelvin. The variable, dn/dT, is the thermo-optic effect of the silicon. The value of n(T) for silicon is $3.49+1.818 \cdot 10^{-4}T$ such that T is the temperature of the silicon.

Studying the basis of electromagnetism allowed us to understand what goes on in the vibration and temperature sensors. Up to now, the propagation of light though fiber is a linear, uniform and isotropic, thus it is not necessary to observe complicated ideas such as ordinary and extra-ordinary waves. The issues that need to be observed throughout the research are the cladding modes and the Fabry-Pérot effects. Later on, these issues will be addressed and there were some solutions to solve these issues.

3 Signal Processing

For both the temperature sensor and vibration sensor, the raw data are recorded as an optical power level as a function of time. In the case of the vibration sensor, a representation of the raw data seldom givers a clear picture of the nature of the vibrations being measured. A much clearer picture emerges when the data are converted from the time domain to the frequency domain via Fourier transform techniques. Figure 3.1.1 shows a hypothetical time trace and the frequency spectrum that results from Fourier transforming that signal. The latter is a much more useful representation of the phenomena being measured[30].

3.1 Frequency Domain

The signals are converted using a fast Fourier transformation (FFT) algorithm. The FFT computes the discrete Fourier transform. In short, the computer collects the information at a regular time interval (Δt) and collects a number of points, N. The total period T equates to N·Δt. Thus, the equations for FFT are the following[31]:

$$A_n = \frac{2}{N}\sum_{r=1}^{N} y(r\Delta t)\cos\left(\frac{2\pi rn}{N}\right) \qquad n = 0,1,\ldots,\frac{N}{2} \tag{3.1}$$

$$B_n = \frac{2}{N}\sum_{r=1}^{N} y(r\Delta t)\sin\left(\frac{2\pi rn}{N}\right) \qquad n = 0,1,\ldots,\frac{N}{2}-1 \tag{3.2}$$

$$y(t_r) = \frac{A_0}{2} + \sum_{n=1}^{N/2-1}\left[A_n\cos\left(\frac{2\pi rn}{N}\right) + B_n\sin\left(\frac{2\pi rn}{N}\right)\right] + \frac{A_{N/2}}{2}\cos(\pi r) \tag{3.3}$$

A_n & B_n : *Fourier coefficient*

N: Number of Samples

Δt : *Time Interval*

An example of a discrete Fourier transformation is shown below:

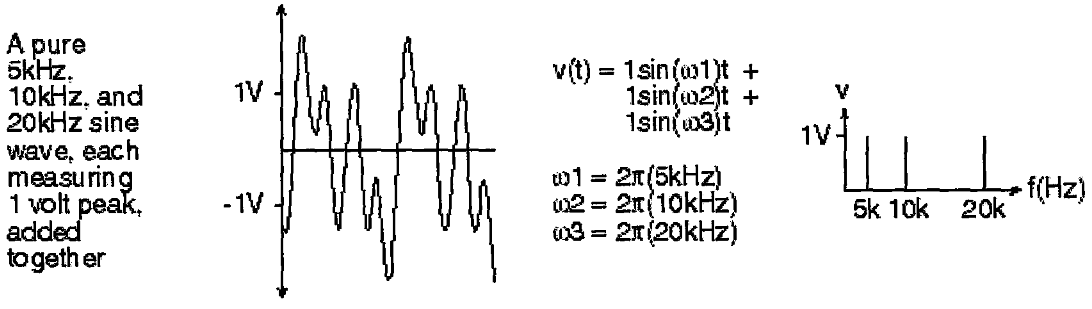

Figure 3.1.1: Voltage signal in the time-domain and in the frequency-domain[32]

3.2 Resolution

The analog outputs from the detectors in the signal and reference channels are digitized using the analog-to-digital converter in the data acquisition (DAQ) board. The DAQ board is from National Instruments, model number NI PCI-MIO-16XE-50. We can control the frequency resolution by two key factors: sampling rate (f_s) and the number of samples (N) recorded[33].

The sampling rate is the frequency at which the samples are recorded. As the number of samples increase while the sampling rate stays constant, the resolution increases. In order to resolve a particular frequency, the sample rate must be at least twice that frequency: $f_s = 2f$. There is frequency limit for a given sampling rate. This is called the Nyquist frequency and it is half the sampling rate: $f_{Nyq} = f_s/2$. The frequencies that are lower than the Nyquist frequency are measured. The frequencies above the Nyquist frequency will appear incorrectly "as lower frequencies in the discrete sample."[33]

In the FFT, there is a fundamental frequency which is the lowest frequency in a full wave that fits in the sampling period. The fundamental frequency is calculated by the following[34]:

$$f_{lowest} = \frac{1}{T} = \frac{1}{N\Delta t} = \frac{f_s}{N} = \Delta f \qquad (3.4)$$
$$\frac{2f_{Nyq}}{N} = f_{lowest} \rightarrow f_{Nyq} = \frac{f_{lowest}N}{2}$$

The Δf represents the smallest possible measurable frequency increment in the frequency domain[34].

3.3 Aliasing

In signal processing, if the data contain frequency components that are higher than the Nyquist frequency, aliasing will occur. Aliasing is an issue in most signal processing situations, including in vibration analysis. When the sampling rate is too low, the FFT will miss certain frequencies and cause a misinterpretation in the frequency spectrum[33]. An example of aliasing is shown below.

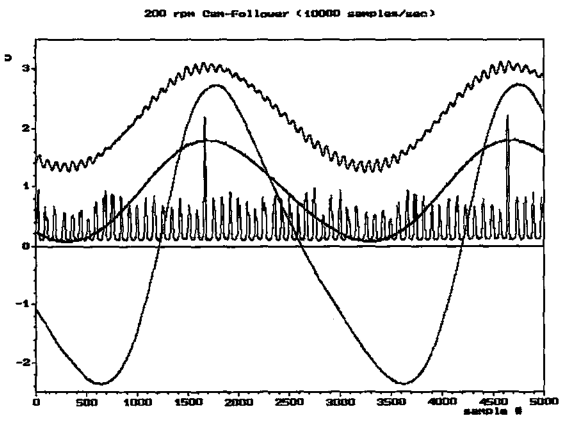

Figure 3.3.1: Correct Sampling Rate[35]

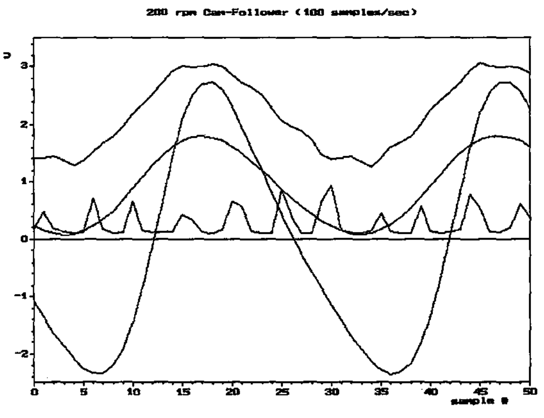

Figure 3.3.2: Under sampling[35]

The issue with aliasing in this research is not necessarily the under-sampling, it is how the data acquisition quantizes the signal[36]. Normally, the equipment temporally quantizes the signal according to the sampling rate. For example, if the sampling rate is 1000Hz, the equipment records the voltage every 1ms; if it is 1400Hz, the equipment records the voltage every 0.714ms.

The following two examples show how the signal in the time domain can change with different sampling rates:

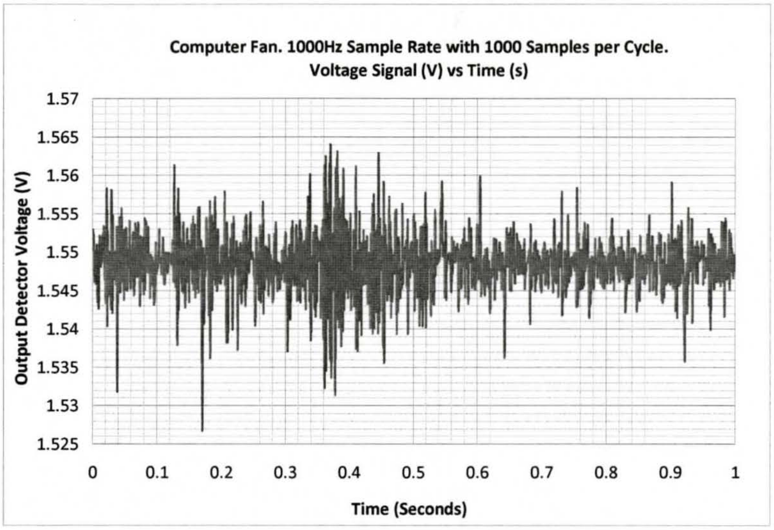

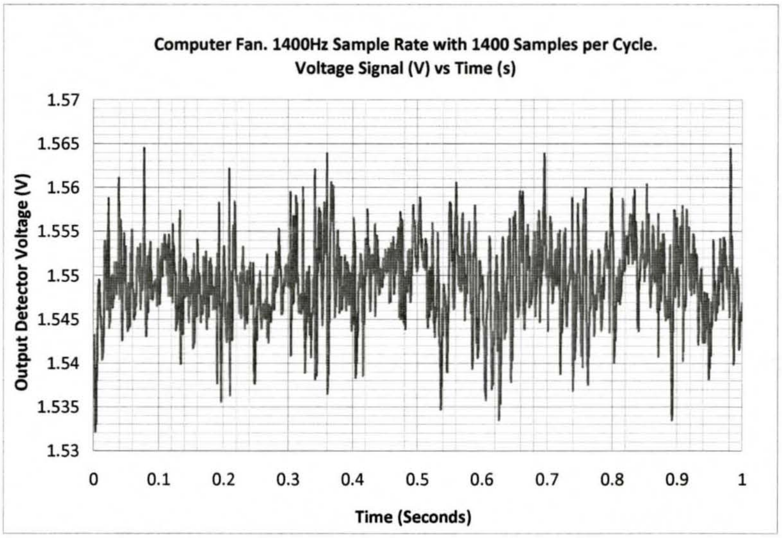

Figure 3.3.3: Two signal traces of the sensor on the boxer fan at two different sampling rates

The two measurements of the same vibration signal are qualitatively different, depending on the sampling rate. To solve this problem, we can take two traces, one at low frequency, around 1000Hz, and one at high frequency, around 10,000Hz, and then overlap the two signals to see which peaks are common in the two traces.

Aliasing is an important issue in the vibration sensor because of the digitizing of the signal. In practice, it is important to vary the sampling rate. Spectral features that appear at some sampling rates and not others are often artefacts due to aliasing.

4 Design, Fabrication and Packaging

4.1 Design of the Temperature Sensor

The temperature sensor is based on the fact that the transmission of light through a piece of silicon is highly temperature dependent for wavelengths near the bandgap wavelength. Essentialy, the sensor is built using a silicon platform with V-grooves to facilitate fiber alignment. The sensing element is a separate silicon slab inserted between two fibers. The design is shown below:

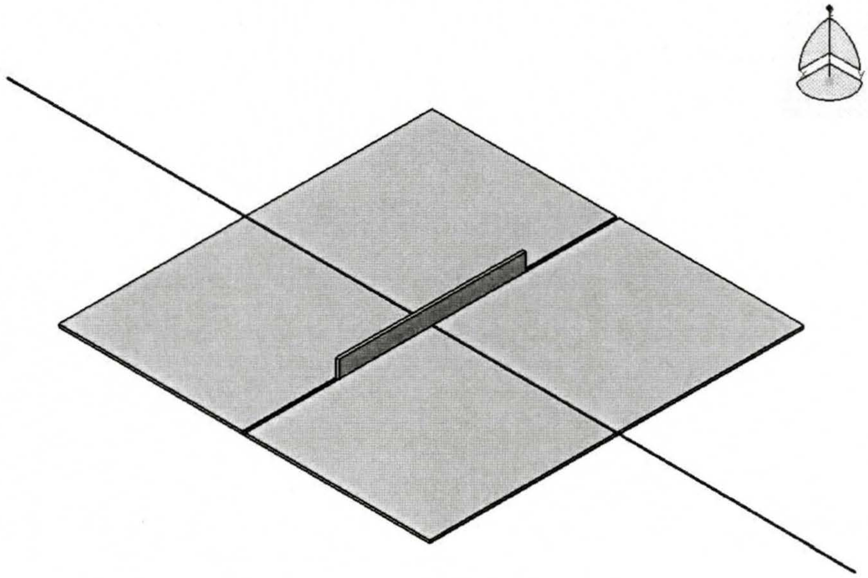

Figure 4.1.1: Silicon Optical Platform Layout

Commercially obtained silicon samples with etched V-grooves were used. An approximate 340µm wide slot was sawn perpendicular to the V-grooves to a depth of about 200µm using a mechanical dicing saw. A 340µm thick piece of silicon, polished both sides, was inserted into the slot. The details of the fabrication of the temperature sensor are given in section 4.3.1.

4.2 Design of the Vibration Sensor

The vibration sensor is a simple cantilever beam. The length of the beam and the initial position of the beam are the main factors determining the quality of the sensor. The actual design of the platform is very simple, as shown below in figure 4.2.1:

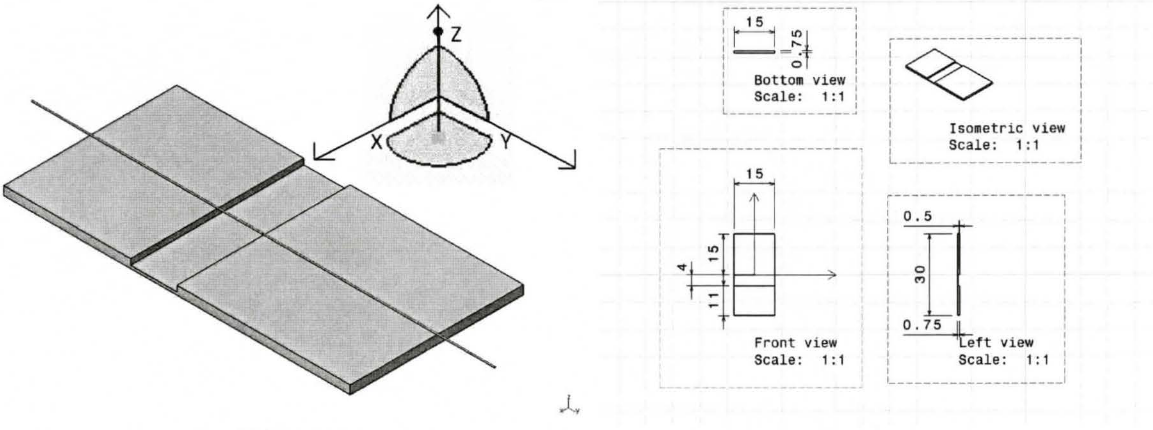

Figure 4.2.1: Drawing of the Vibration Sensor (dimensions in mm)

The design of the cantilever is very basic with two fibers extending certain lengths into the gap. The right fiber is the output to the detector; the length protruding into the gap is made as short as possible to ensure stiffness. The left fiber is the input from the laser; the length of the cantilever portion depends on the design. The gap between the two fibers must be small enough such that most of the light exiting one fiber will be captured in the core of the other fiber. The details of the fabrication of the vibration sensor will be explained in section 4.3.2. The compass in the figure indicates the coordinate system that is used throughout the thesis.

Designing the vibration sensor requires consideration of two factors: laser's wavelength and the fiber cantilever's length. The fiber's length, basically a cantilever beam design, determines the natural frequency and the sensitivity of the system.

4.2.1 Wavelength Selection

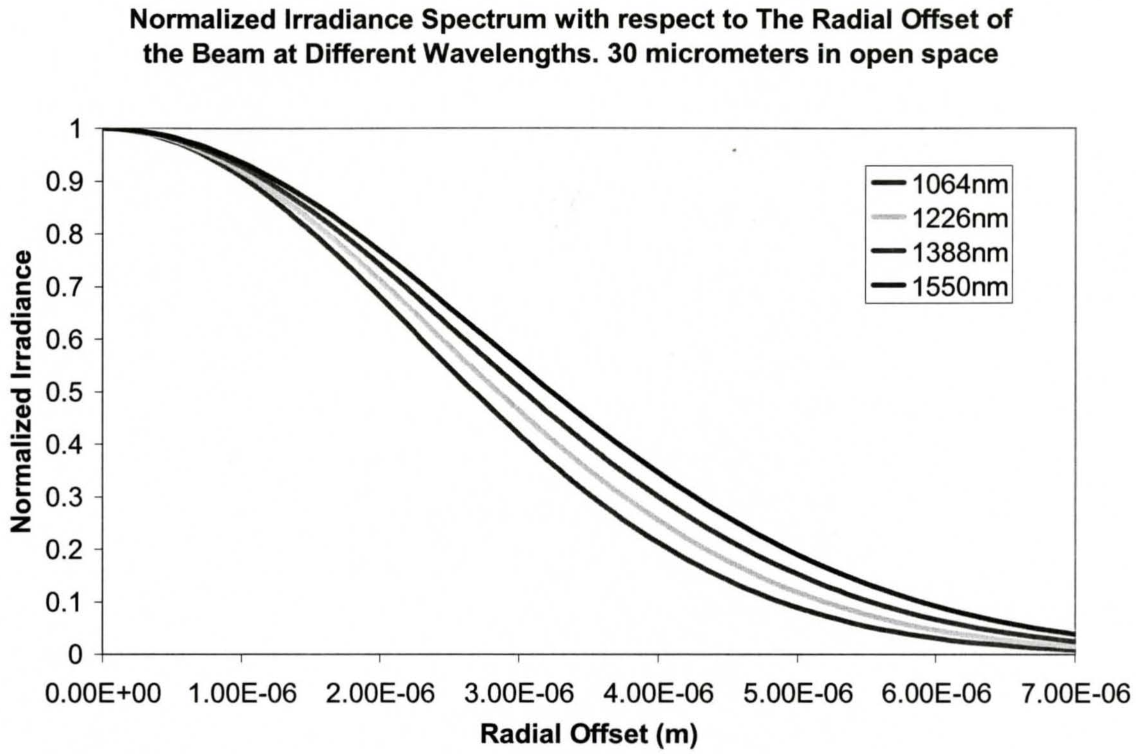

Figure 4.2.1.1: Intensity (Irradiance) of the Gaussian Beam with Respect to Radial position.

Figure 4.2.1.1 shows the relative intensity distribution of the light that exits the fiber, assuming Gaussian beam configuration. Unlike the temperatures sensor, the choice of the wavelength is not very critical. It was a matter of practical convenience in this work to use the same laser source for both. The shorter the wavelength is, the sharper the slope of the intensity distribution is. This can be useful for increasing the sensitivity of the vibration sensing. This graph shows that choosing the 1064nm laser is a slightly better choice than the 1550nm for the vibration sensor.

The Gaussian beam equation from section 2.3.2 is used to analyze the intensity of the beam.

$$I(r,z)=I_0\left(\frac{w_0}{w(z)}\right)^2\exp\left(\frac{-2r^2}{w^2(z)}\right) \qquad (2.35)$$

$$R(z)=z\left(1+\left(\frac{z}{z_0}\right)^2\right) \qquad (2.36)$$

$$w(z)=w_0\sqrt{1+\left(\frac{z}{z_0}\right)^2} \qquad (2.37)$$

$$z_0=\frac{\pi w_0^2}{\lambda} \qquad (2.38)$$

The beam waist radius, w₀, is assumed to be the fiber core radius of 3.5µm for simplicity. The axial distance, z, is 30µm from the beam waist since the receiving fiber end is at that distance. Thus, the development of equation 4.1 is shown below:

$$I(r,\lambda)=\frac{1.633\cdot 10^7\cdot\exp\left(-\frac{1.633\cdot 10^{11}r^2\pi^2}{\pi^2+6\cdot 10^{12}\lambda^2}\right)\cdot\pi^2}{\pi^3+6\cdot 10^{12}\lambda^2} \qquad (4.1)$$

Equation 4.1 is not normalized; therefore, dividing equation 4.1 by itself replacing the radial offset to zero, the normalized equation results in the following:

$$I_n(r,\lambda)=\exp\left(-\frac{1.633\cdot 10^{11}r^2\pi^2}{\pi^2+6\cdot 10^{12}\lambda^2}\right) \qquad \mathit{(4.2)}$$

4.2.2 Cantilever Beam Design

Designing the cantilever beam can be complicated. We have to consider many factors and different designs. During the designing stage, we look at two different configurations: a straight beam that bends under its own weight and a straight beam with a seismic load to increase the sensitivity. There are several parameters to consider when designing a cantilever beam for the vibration sensor. The parameters are the following:

- Young's Modulus of Elasticity
- Geometric Moment of Inertia
- Length of the Beam
- Force applied to the Beam

The main purpose of this design is to develop a vibration sensor that detects the acceleration of the platform on which the fibers are mounted. In order to start developing an accelerometer, we have to use the basics of mechanical vibration as stated in section 2.2.3. We will look at the first case with a straight beam with no seismic load. The equation necessary for the development of cantilever beam is:

$$\omega_n = \sqrt{\frac{8EI}{\rho L^4 A}} \qquad (4.3)$$

Now, when we plug in the following values (note that d is fiber diameter and it will be the variable):

- Young's Modulus (E) = 71.7GPa
- Geometric Moment of Inertia ($I = 1/64 \cdot \pi d^4$) = $15.625 \cdot 10^{-3} \pi \cdot d^4$ m^4
- Density (ρ) = 2200 kg/m^3
- Area ($A = ¼ \cdot \pi d^2$) $0.25\pi \cdot d^2$ m^2

$$\omega_n = 4036.763\sqrt{\frac{d^2}{L^4}} \qquad (4.4)$$

So we have an optimization problem. We can graph how the natural frequency changes in terms of length and at different diameters of fiber. We needed to determine the diameter of our cantilever beam.

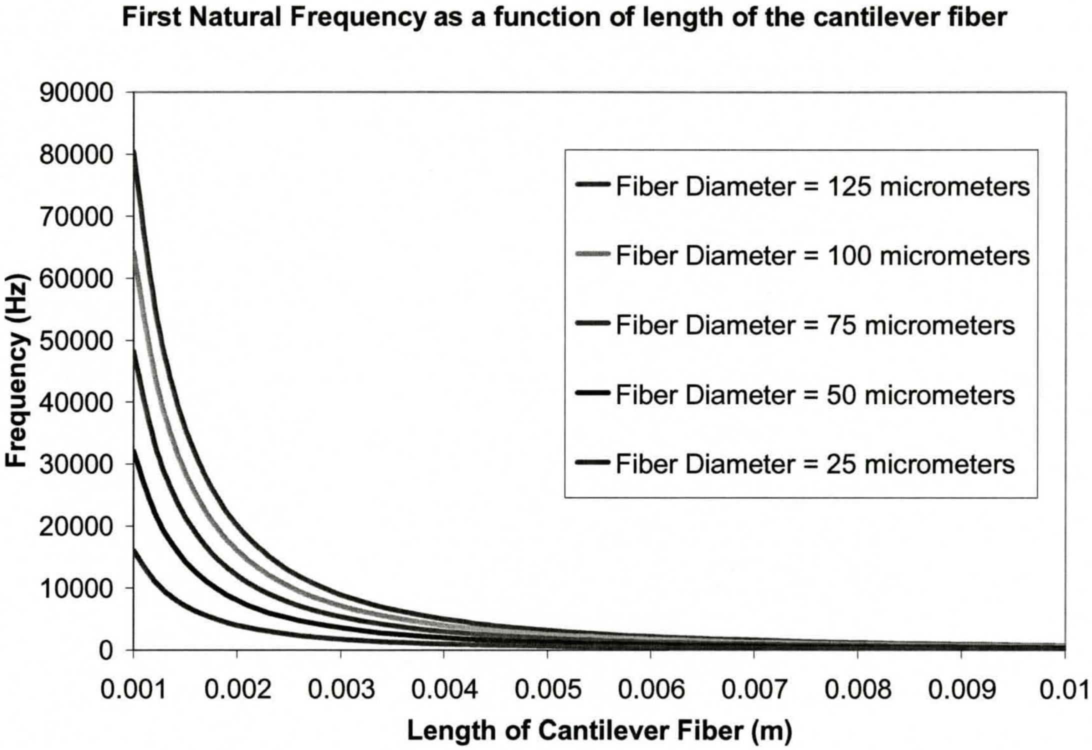

Figure 4.2.2.1: First Resonance Frequency as a Function of Length at Different Frequencies

From this graph, we can see that the shorter the fiber is, the larger the natural frequency of the system. The larger the diameter of the fiber, the higher the resonance frequency is. Now, we must look at the amount of deflection in the fiber in terms of length. From the deflection formula in equation 2.22.iv in Chapter 2 and inserting the values for the natural frequency and diameter of the fiber, we have this derivation:

$$s(t) = Se^{-\zeta\omega_n t}\left(\cos\left(\omega_d t\right) + \cos\left(\omega_d t\right)\right) + \frac{Y_{base}\cdot r^2}{\sqrt{\left(1-r^2\right)^2 + \left(2\zeta r\right)^2}}\cos\left(2\pi f t - \arctan\left(\frac{2\zeta r}{1-r^2}\right)\right) \quad (2.22.iv)$$

$$\text{Such that } s(t) = y_{\text{sensor}}(t) - y_{base}(t),\ r = \frac{f}{f_n},\ \zeta = \frac{c}{c_c} \text{ and } \omega_d = \sqrt{1-\zeta^2}\,\omega_n$$

From equation 2.22.iv we will take the graph of the relative deflection with respect to frequency. This creating the following graph:

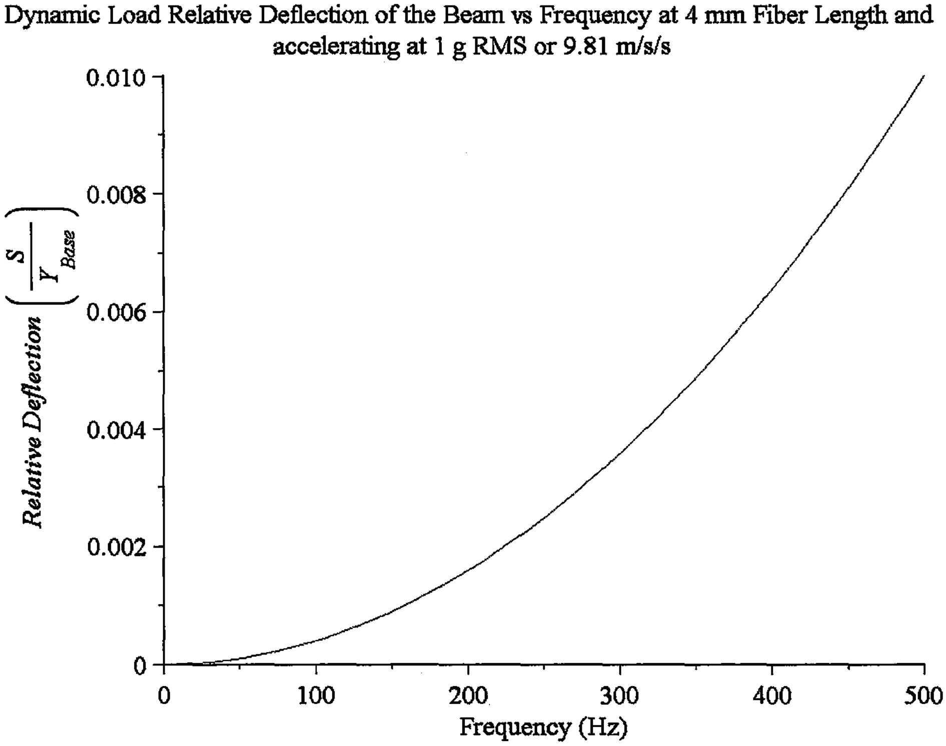

Figure 4.2.2.2: Dynamic Load Relative Deflection in respect to Frequency

$$S = Y_{base}\frac{(2\pi f)^2}{(2\pi f_n)^2} = \frac{\ddot{Y}_{base}}{(2\pi f_n)^2} \quad (4.5)$$

At 100Hz, the relative deflection comes to 397.09µm/µm. The displacement of the vibrating object (Y_{Base}) at 1g RMS is 24.85µm. Using the relative deflecting value and the displacement of Y_{Base}, the deflection of the cantilever fiber, S, is 9.86nm. This is enough deflection when we use single mode to single mode connection; the reason is that we are detecting the vibration via riding the Gaussian beam edge. However, with a single to multi mode fiber, the sensitivity decreases significantly.

With the theoretical value of 9.86nm dynamic deflection, this must be verified that this is accurate.

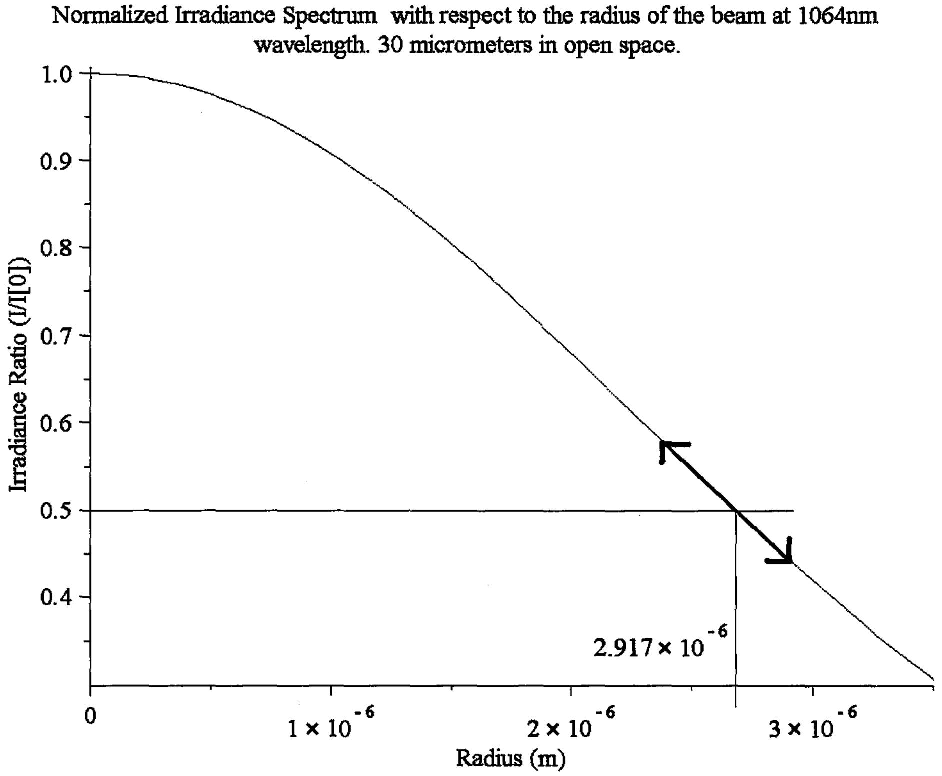

Figure 4.2.2.3: Intensity (Irradiance) of the Gaussian Beam with Respect to Radial position.

At 50% power, ideally, there is an offset of 2.917µm between the two fibers. Note that the 50% power is the DC voltage of the sensor. The arrows in figure 4.2.2.3 represent the area of detection for vibration. Using the deflection value of 9.86nm, the area of detection is from 2.90713µm to 2.92687µm. Converting back to intensity ratio, the area of detection is from

0.502454 to 0.497765 (unit-less). These two values will be compared with the experimental data.

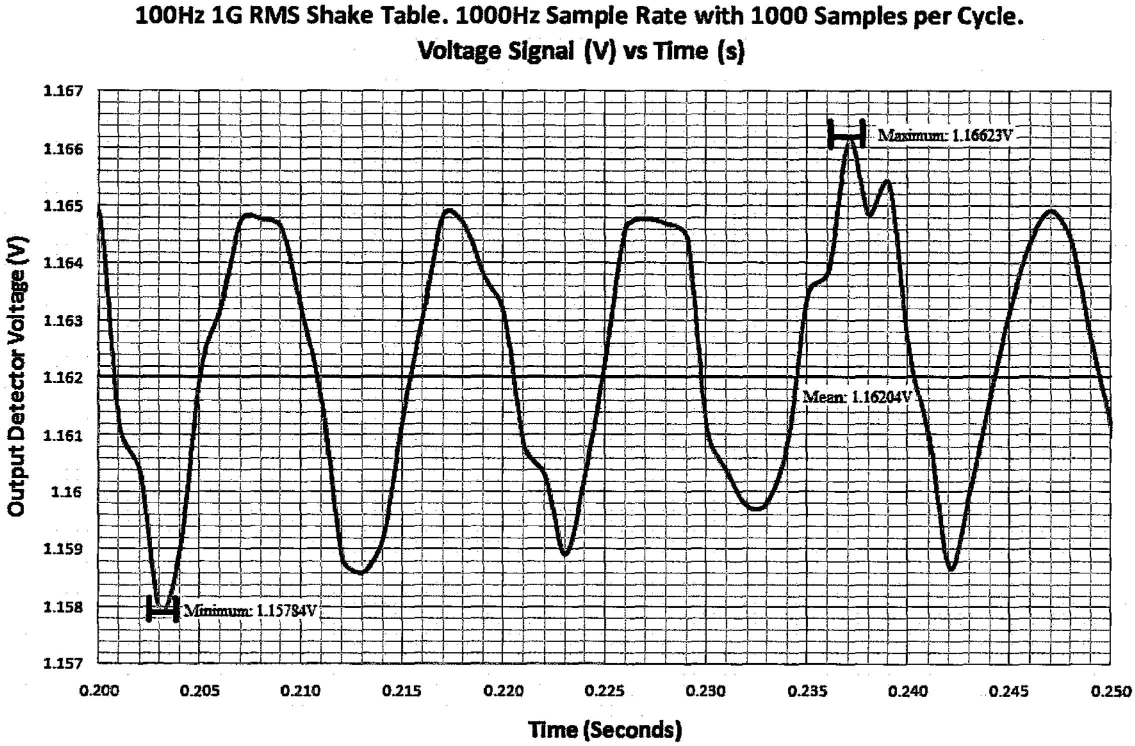

Figure 4.2.2.4: Experimental Data of the Vibration Sensor

Calculating the voltage range at 100Hz and at 1g RMS, the power percentage range is from 0.50181 to 0.49819. The error from the theoretical to the experimental is at 0.13; thus these calculations are accurate.

Now we will look at the second case in which there is a seismic load on the cantilever beam. The seismic load is a fixed spherical mass, assuming the material is the same as the cantilever (SiO_2), which is at the end of the fiber cantilever.

When it comes to calculating the natural frequency, we must add the effective mass of the bar and the seismic mass. The effective mass represents the equivalent point mass at the end of a massless bar. For a weighted cantilever bar, the effective point mass is 0.22348 times the mass of the bar. Thus we will get the following equation and graph:

$$\omega_n = \sqrt{\frac{3EI}{L^3} \cdot \frac{1}{\left(\frac{4}{3}\pi \rho r^3 + 0.22348 \rho L A\right)}} \qquad (4.6)$$

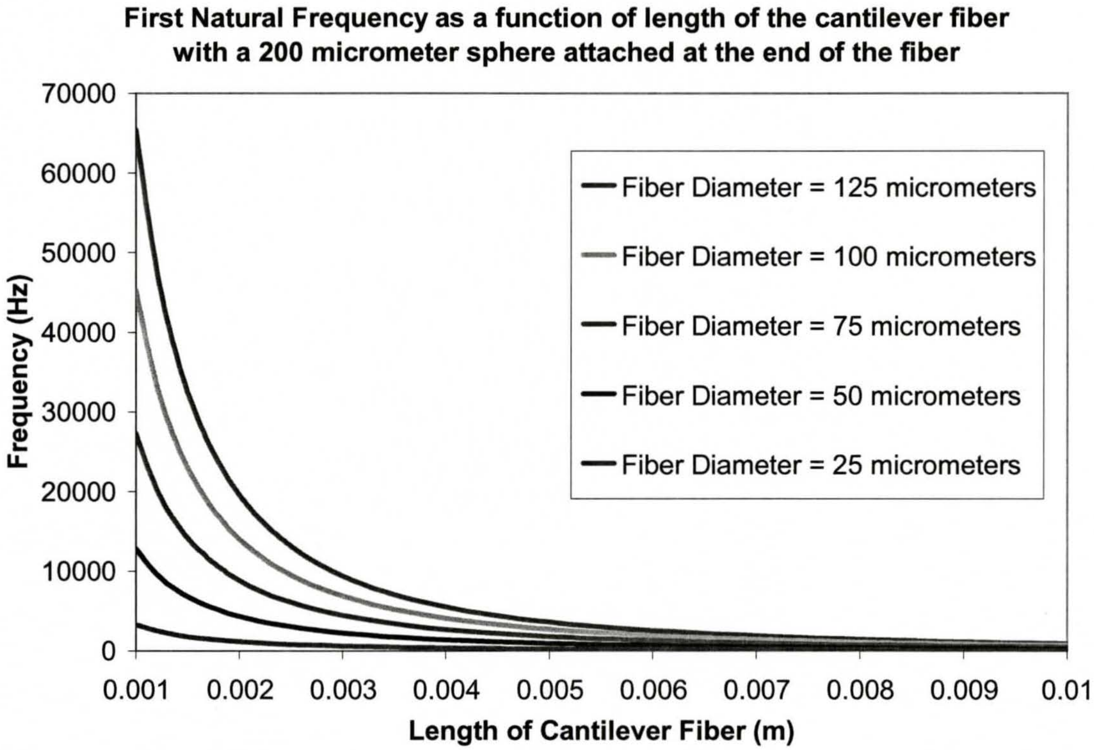

Figure 4.2.2.5: Resonance Frequency Spectrum according to a massed cantilever beam with a seismic load

The seismic load does decrease the natural frequency in comparison to the distributed load, albeit the moment of inertia did not change in this manner. The gross underestimation of having the moment of inertia the same while having a seismic load can seriously alter the results.

Using equation 2.22.iv from chapter two with the change of the natural frequency, the dynamic load relative deflection with respect to frequency is shown in graph 4.2.2.6.

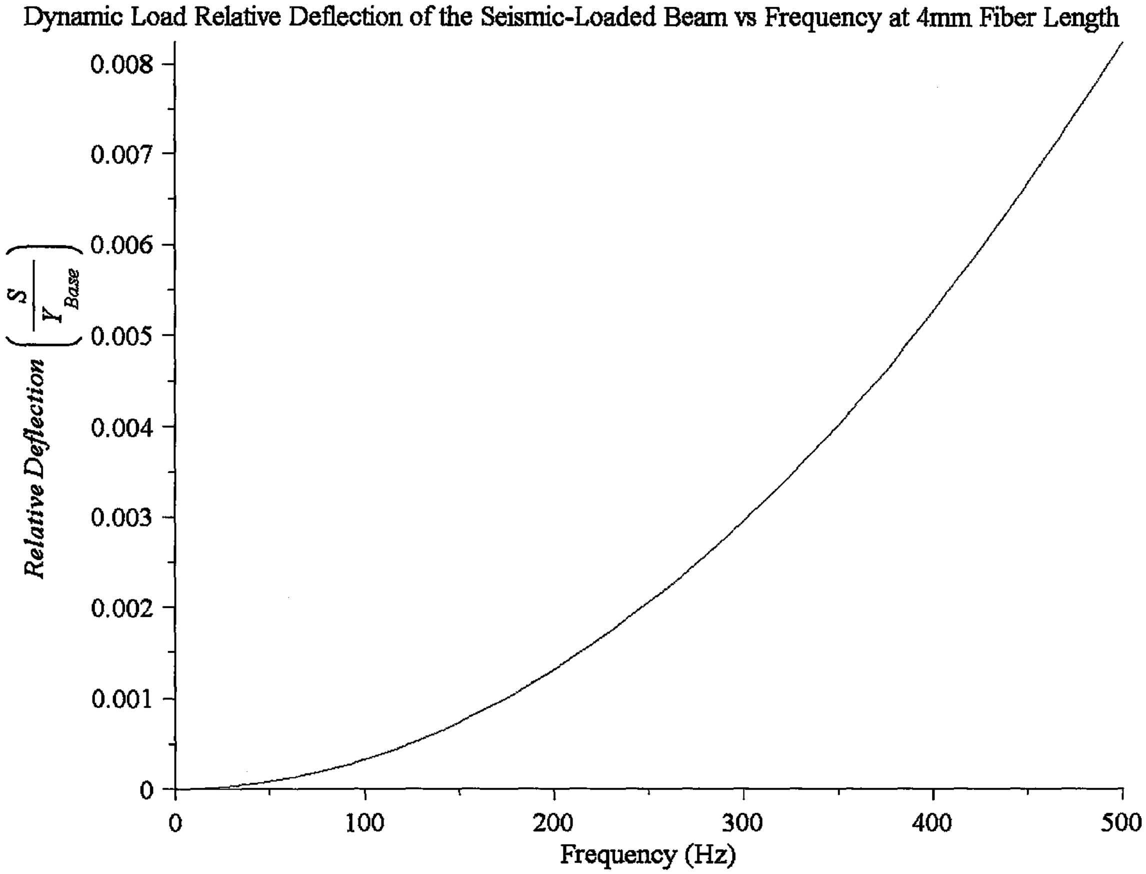

Figure 4.2.2.6: Dynamic Load Deflection Load Deflection with Seismic Mass in respect to Length of Fiber at Different Accelerations

In conclusion, having a seismic mass actually gives more problems than it solves. Although it gives a higher sensitivity, the natural frequency decreases significantly. This will restrict development of a decent vibration sensor. Hypothetically if adding a seismic mass gives a higher natural frequency and better sensitivity, the time consumption of fabrication will become a factor. Finally, I thought that it was not worth developing a seismic massed cantilever beam for the intended application.

4.3 Fabrication

4.3.1 Temperature Sensor Fabrication

The fabrication of the temperature sensor involves a purchased V-groove platform, a 337µm silicon slab, one 1/8 inch aluminum slab, SMF-980 patch cord rated at 1064nm, two stages and a stand.

The first step is to take the V-groove platform and saw a slot 340µm across. Then, take an aluminium slab and cut a piece 1.25"x0.75" to have a good fit in the box when packaging. After grinding the edges and cleaning the aluminum block, we epoxied the V-grooves silicon platform on top of the slab. Then we placed the silicon slab into the 340µm slot of the platform. Then the block is placed on a stand in the middle of the two stages.

We cut a patch cord, SMF-980 model, into two equal pieces. Then cut back the protective tubing to expose 100mm of the jacket and 6mm of stripped bare fiber on each half. The power output of the fiber end by cleaning and cleaving it and then inserting the bare fiber into a detector. The laser delivers 200µW from the splitter with the optical isolator. The typical output power was around 160µW. The fibre was cleaved again at the shortest length possible to minimize the amount of the jacket, which was about 3mm. The reason is to have the sensor as close to the edge of the box as possible. After cleaving, the input patch chord is placed on one stage. From the output patch cord we removed 60mm protective tubing. The reason is to have a strain relief for the bare fiber when it bends around inside the aluminium box. The fiber end is cleaved and cleaned at a 10mm length. Then it is placed on top of the second stage. This patch cord is then connected to a detector.

So there are two halved patch cords on two stages with the V-Grooves in the middle. The two fibers are lowered into the grooves. We carefully monitor the power while aligning the fibers to get the maximum throughput. Initially, we obtained the maximum power of 3µW; once we carefully place the Norland 61 optical epoxy on the fibers, the power increases to 10µW. The adhesive was left to cure for five minute with a 340nm wavelength UV gun; after the curing, the power rose to about 16µW which is 1/10 of the input power, which we expected. Finally, we placed the sensor on a hot plate for further curing overnight at 50^0C.

4.3.2 Vibration Sensor Fabrication

The vibration sensor fabrication is similar to the temperature sensor in terms of the slab placement and the fiber cleaving; however, from there, the process of fabrication diverges. The temperature sensor uses V-grooves while the vibration sensor uses a flat silicon platform. The silicon platform is 30mm long, 15mm wide and 750µm deep. The components needed for fabrication are the silicon vibration platform, patch cord rated at 1064nm, a 1/8 inch aluminum slab, one mechanical stage and one piezostage.

We cut a groove into the 750µm thick vibration platform 200µm deep and 4mm wide because we want approximately a 4mm cantilever beam. Then, again, we cut the aluminum slab 1.25"x0.75", grind the edges and clean. Then we placed the slab onto the piezostage.

We prepared the two halved patch cords (the dimensions are the same for both sensors, as well as the same power output); we placed the fiber on top of the platform extending it to nearly 4mm into the gap. Then, we placed the adhesive, cured it and rotated it to the other end. We placed the second halved patch cord on top of the platform facing the other fiber. The second halved patch cord is extremely short, about 3mm of stripped bare fiber.

Before applying the adhesive, we align the fiber to get the maximum throughput and then we offset the second fiber to reduce the power throughput by one half according to equation 5.2.2. Lastly, we put on the Norland 61 epoxy and cured it for five minutes with the UV gun.

4.4 Packaging

4.4.1 Single Sensor Head

The packaging for both the temperature and vibration sensor are identical. What is involved is a standard cast aluminum box of 2.475"x2.25"x1.25" purchased from electronics supplier Digikey, heat-cured epoxy, silicone caulking and various aluminum slabs. The process is straightforward.

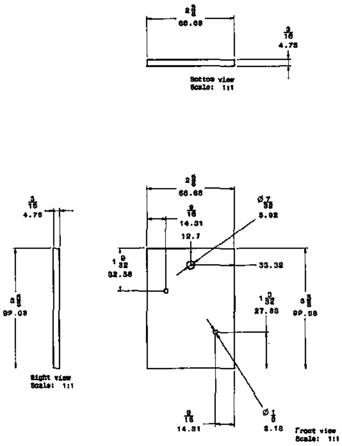

Figure 4.4.1.1: Mechanical Drawing of the Aluminum Slab

First, we milled a slot on the box, 3/16 inches in width. Then we cut an aluminum slab 3.625"x2.625" and drill, tap and screw two holes from the base of the slab to the block to hold it in place as placed in figure 4.4.1.1. Then we drilled a 1/4-inch clearance hole at the edge of the aluminum slab for holding the sensor head.

The second part was the most difficult, putting the sensor in the box. We applied the heat curing epoxy to the box, lowering the sensor in the box while the other fiber is hanging loosely. Then we bend the other fiber such that it comes out the same slot as the input fiber and then we tack down the fiber with the silicone to secure it. We use tie-wrap strips to secure the outside fibers six to seven inches outside the box for further strain relief

We used the silicone caulking to seal the outside fibers. In addition, we put an aluminum cap and sealed it with the silicone caulking again. Finally, we caulked the rest of the opened slot of the box.

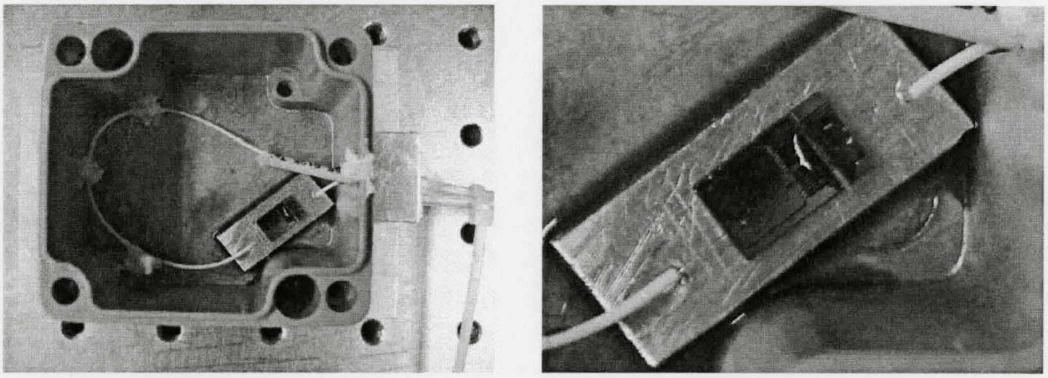

Figure 4.4.1.2. Packaged Temperature Sensor

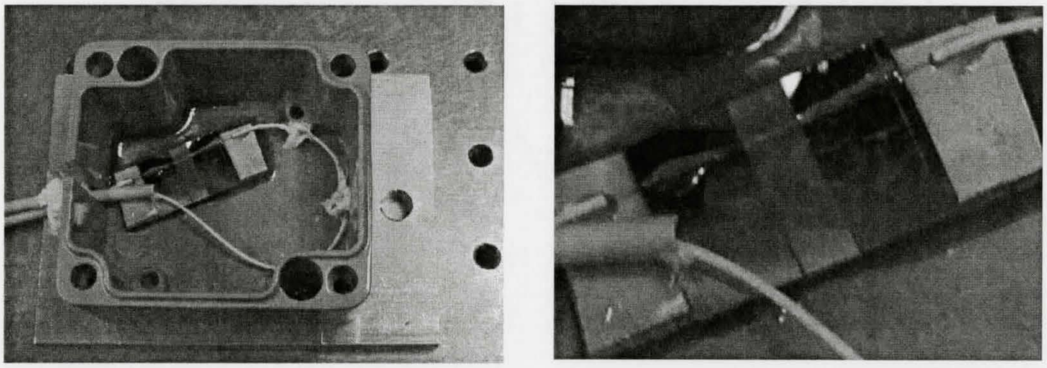

Figure 4.4.1.3. Packaged Vibration Sensor

4.4.2 Dual Sensor Head

The dual sensor head was not packaged; however, the packaging for a dual sensor head would have the same procedure as the single head. The main difference is having two sensors in one box instead of two. The box has the same dimensions as the single sensor heads. All the steps remain exactly the same throughout with the exception of putting the silicon caulking to the remaining slot; note that the temperature sensor will be the first one entering the box. After the first sensor is in the box and secured, we place a metal plate on top of the sensor without touching. The metal plate will be sealed via weld for a firm secure (epoxy could come loose at high temperatures). Then we follow the same procedure as with the first sensor, place the glue on top of the plate and bend the fiber around; at the same time, tacking the fibers on the edges with the silicone caulking. After, it is the same procedure as before: use tie-wrap to tighten the outside fibers six to seven inches outside the box for further strain relief, use the silicone caulking to seal the outside fibers, putting aluminum cap, seal and put caulking onto the rest of the openings of the box.

5 Temperature Sensor Results

5.1 Preliminary Experiments Using Silicon Piece Inserted into Fiber-to-Fiber Connector

Initially, I used a fiber-to-fiber connector with a small piece of silicon inserted between the two ceramic tips of FC conectors.

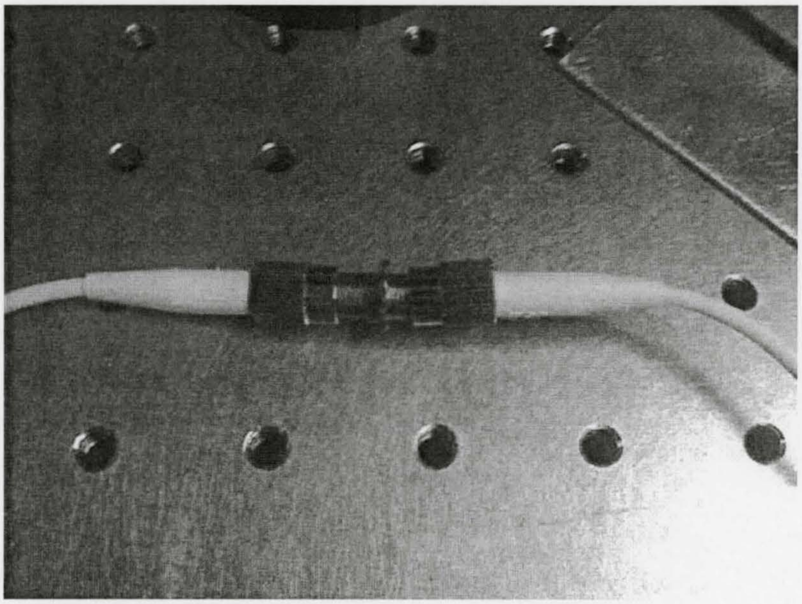

Figure 5.1 1 Fiber-to-Fiber Connector Sensor

The purpose of the experiment was to test the theory behind the silicon filter technique. There were numerous tests performed to validate the absorption edge theory. There were three main configurations done with the experiments:

1. Immersion: Placing the sensor in a beaker of water and heating it to different temperatures.
2. Heating Through Convection: Having a heatgun blowing on the sensor

3. Hot Plate Conduction: The configuration of choice due to Dofasco's requirements.

55mA is the current used for the laser output, rarely varied since 55mA is the current at which the laser is at its best output.

5.2 Immersion Experiment

The immersion experiment carried on August 16, 2007, demonstrated how closely the theoretical and experimental transmission results agreed. The experiment consisted of three tests:

1. Temperature rises from 20^0C to 150^0C, and then falls back to 20^0C, according to the hot plate. 25 samples per cycle.
2. Temperature rises from 20^0C to 150^0C, and then falls back to 20^0C, according to the hot plate. 50 samples per cycle.
3. Temperature steps, in Celsius: 27, 60, 100, 140, 60, 34; all according to the hot plate. 50Hz sample rate at 50 samples per cycle.

The data from the second test are shown in figure 5.2.1a, b and c. The first graph shows the relative transmission ratio versus time to observe the relation between the voltage and the temperature. The second graph shows the relative transmission versus temperature. The temperature in that graph is from the water using a thermometer. The purpose of the second graph is to compare with the theoretical curve of equation 2.7 (when normalized at 25^0C) in section 2.1.

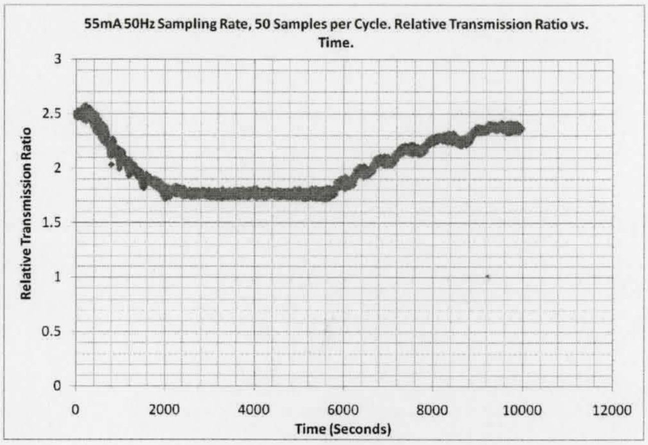

Figure 5.2.1a. Second Immersion Test.

Normalized Transmission Ratio vs. Time.

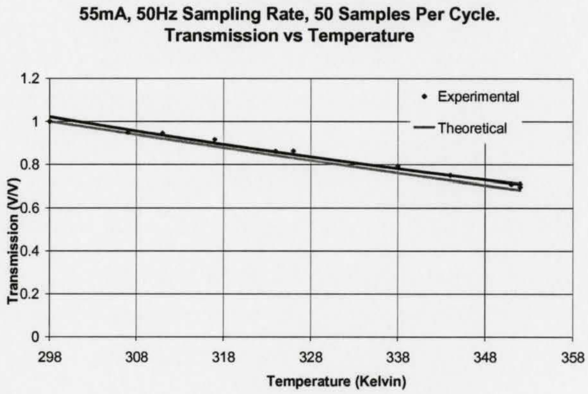

Figure 5.2.1b: Second Immersion Test.

Transmission vs. Temperature

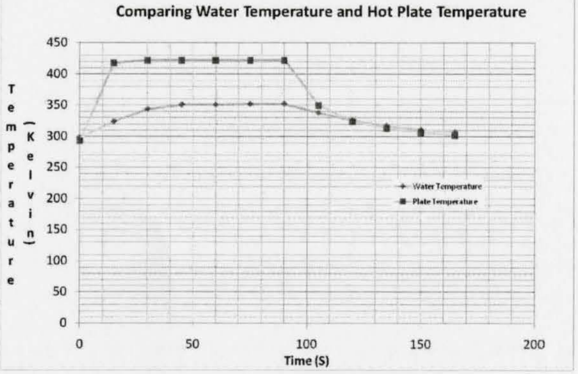

Figure 5.2.1c: Second Immersion Test.

Water Temperature and Hot Plate Temperature vs. Time

5.3 Heat Convection Test on September 3, 2007

I conducted convection tests to determine the response time of the sensor As expected, the relative transmission dropped with an increase in temperature:

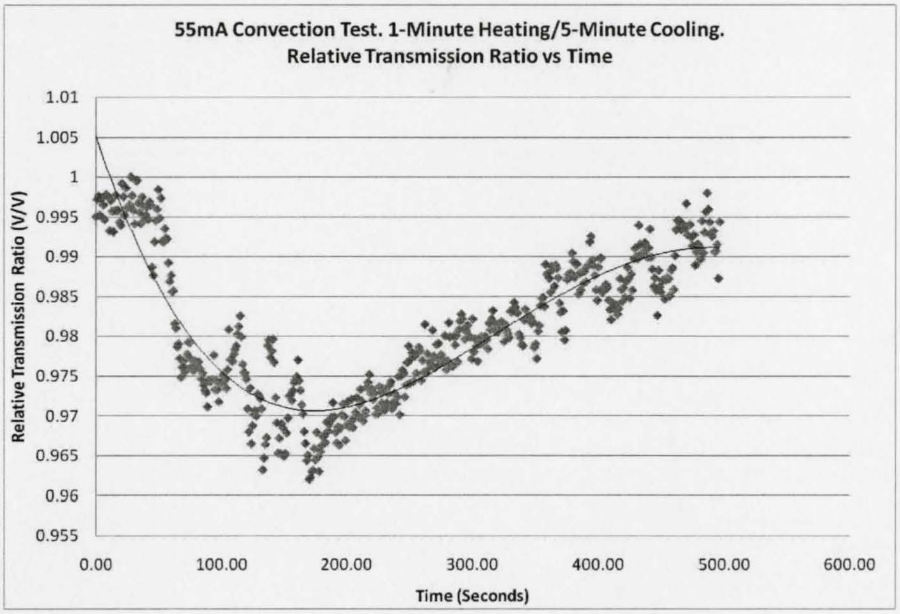

Figure 5.3.1 Heat Convection Test. 1-Minute Heating and 5-Minute Cool Down. This was performed on September 3, 2007

After the preliminary water and heat gun testing, more controlled testing techniques using the hot plate was carried out. The hot plate gives a reasonable approximation of the intended application at Dofasco. Thus, conduction is the major key for the success of the sensor

5.4 Testing of Sensor Mounted on Silicon Platform

The temperature is inferred from a measurement of relative transmission according to equation 5.1. The equation is normalized to 298K or 25C from equation 2.7 Initially, we picked the K value as 2400 from section 2.1 for a reference. With the use of a calibration table, it was found that K which equalled to 2625 gives the best fit to the data. The TransmissionAt298K constant is the value that normalizes the relative transmission to unity at is 298^{0}K. This value is 0.4674. The A constant is the determining factor of the equation. This shifts according to the calibration of the thermistor Normally, this would be 1, but there must be minor adjustments to comply with the thermistor values. The value of A is 1.0179. Thus with these values, we get a decent fitting curve. The most important factor is that the steady-state temperatures of the two curves fit properly.

$$\text{RelativeTransmission} = A'\cdot \exp\left(-KL\left(\frac{1.24}{\lambda} - 1\ 1655 + \frac{0.000473T^2}{T+\beta} \right)^{\frac{3}{2}} \right) \tag{5.1}$$

$$A' = \frac{A}{TransmissionAt298K}$$

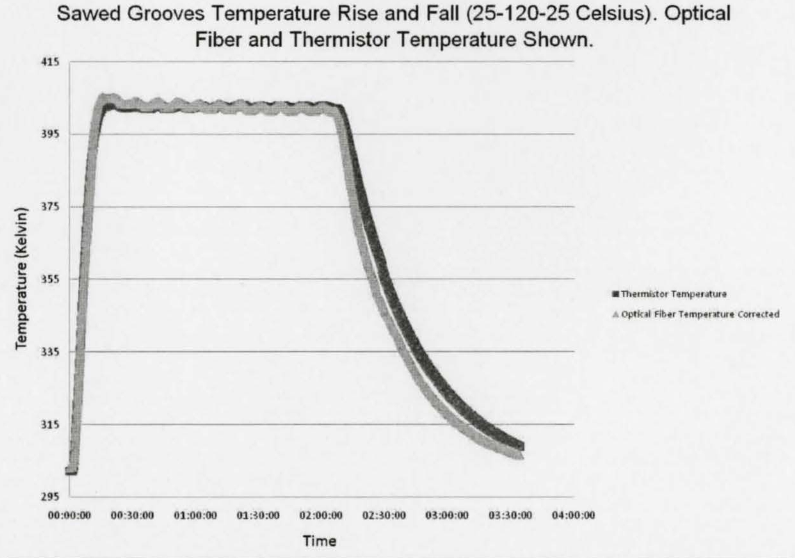

Figure 5.4.1 Sawed Groove Temperature Rise and Fall Conducted on November 22, 2007

5.5 January 7 and 8, 2008 Immersion Test

The sawed-grooves silicon temperature sensor was submerged in a beaker full of water. The purpose was to distribute the heat all over the sensor. During those tests, I put in an optical isolator. The purpose of the optical isolator is to prevent feedback to the laser, which was causing it to become unstable. Unfortunately, there had been numerous problems with the data. The data from the sensor did not follow the data from the thermometer. In the first two experiments, the current from the laser was at 55mA while in the last experiment, it was at 45mA. During the first 55mA test, the stirrer was on at 300rpm, distributing the heat throughout the water; the bridge broke during this trial run, and the stirrer was cancelled. The second 55mA test, the stirrer was not on; and in the 45mA test, the stirrer was on at 50rpm. The results were not satisfactory probably because of the following speculations:

1. The connection between the two fibers are bad and unstable
2. The water seeped inside the glue and changes the refractive indexes in the junction
3. The water changed the properties of the silicon

During the first test, I noticed that there was digitization of the signal. So, for the second and third experiments, I programmed LabView to take the mode of each signal such that the results would improve. The results were not satisfactory because there were vigorous voltage drops and rises. This is due to the improper sawed grooves on the platform. Section 5.6 uses the same sawed grooves in a steady-state environment.

5.6 Steady-State Temperature Experiment on January 11 to 13, 2008

The experiments carried out on January 11 to 13, 2008, regarding the steady-state analysis of the optical fiber sensor in comparison to the thermistor, raised some questions on the repeatability of the tests. The experiment consisted of four tests:

1. 1-hour at 100^0C followed by a 2-hour cool-down period.
2. 20-Hour Test steady-state at 100^0C and 22^0C for 8 hours each with a 4-hour cool-down period.
3. 20-Hour Test steady-state at 120^0C and 22^0C for 8 hours each with a 4-hour cool-down period.
4. 2-hour at 120^0C followed by a 3-hour cool-down period.

The four tests were carried out using the silicon sawed grooves sensor with a maximum power output to the detectors of 5.85μW. The glue was cured via UV gun before each test commenced. Each test has the following curing process (with respect to each test above):

1. 5 minutes; no glue added.
2. Additional 2 minutes; no glue added.
3. No curing.
4. Additional 3 minutes; no glue added.

As well, I put in a process to vary the data collection. For the first test, the program collected data every second for the first twenty minutes; after, it collected data every ten minutes. The other three tests, the program collected data every second for the first ten minutes; after, it collected data every ten minutes. The reason for the initial step was to calibrate the sensor properly. Normally, it would not take ten minutes to calibrate.

The program recorded four different data tables per test: reference arm voltage, test piece voltage, thermistor temperature and optical fiber sensor temperature. The reference arm voltage is recording the signal from the reference channel. The reference arm voltage is needed to calculate the optical fiber sensor temperature. The test piece voltage is recording the signal coming from the silicon platform temperature sensor. This voltage contributes to the calculation of the optical fiber sensor temperature. The thermistor temperature is the control of this experiment and all further experiments in this thesis. The thermistor detects the temperature via resistance change. The optical fiber sensor temperature calculates the temperature from the test piece voltage and the thermistor voltage. The full calculation was explained in section 2.1 and 5.1.

The sensitivity of the temperature sensor is calculated by taking the minimum and maximum peak temperatures of the calibration period. The calibration period, as describe before, is where the temperature of the sensor is at room temperature, and the sensor is inactive. The peak-to-peak temperature is 0.084^0C. There is an uncertainty factor to give a buffer for the sensitivity calculation. The uncertainty factor of five is multiply with the peak-to-peak temperature. The sensitivity of the temperature sensor is 0.4^0C.

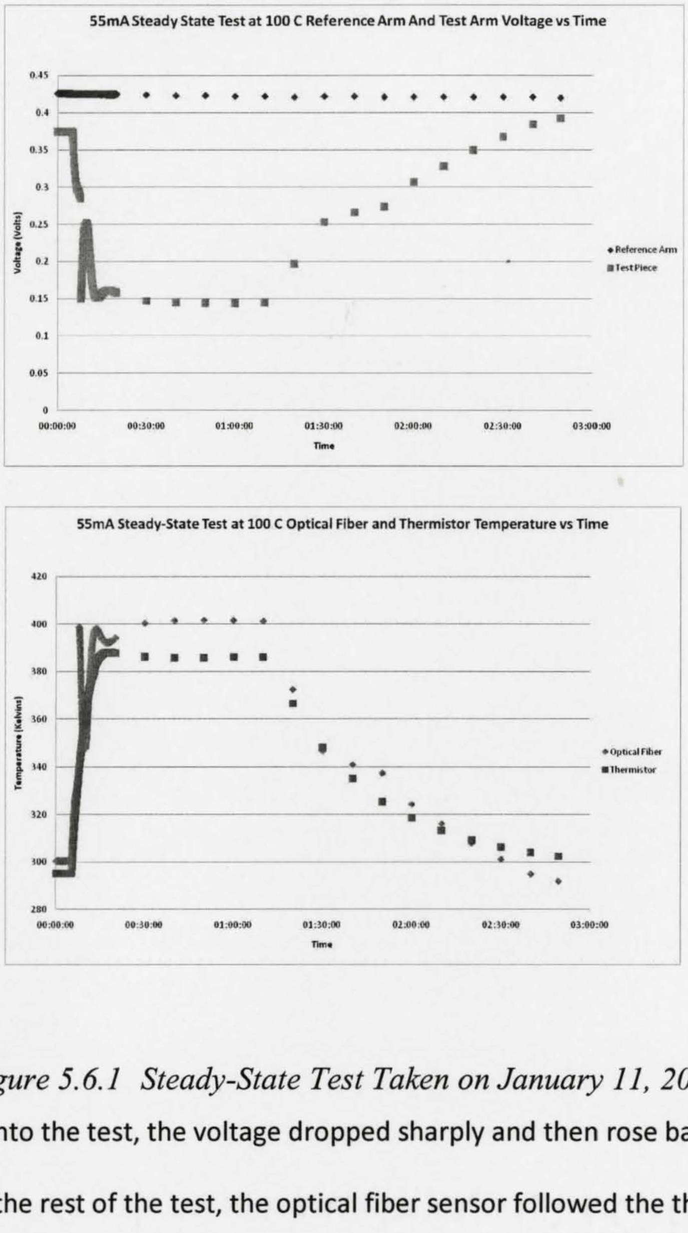

Figure 5.6.1 Steady-State Test Taken on January 11, 2008

Around 8 minutes into the test, the voltage dropped sharply and then rose back up to its original trend. Throughout the rest of the test, the optical fiber sensor followed the thermistor nicely. I thought that it was a curing problem so I cured the sampled for an additional two minutes (mentioned above). After, I did a twenty-hour experiment to see if additional curing would help; the results are shown in figure 5.6.2:

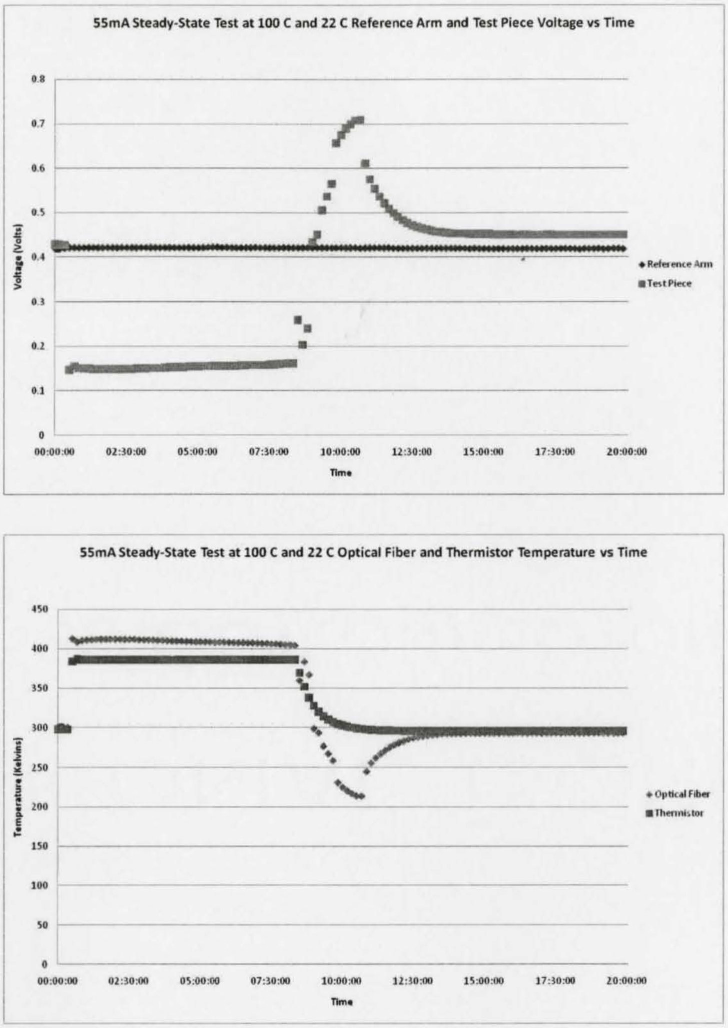

Figure 5.6.2 Steady-State Test Taken Between January 11 and 12, 2008

In steady-state, both at 100^0C and 22^0C, the optical fiber sensor and the thermistor showed approximately the same temperature. The program needed to be recalibrated, which was done on the third experiment. When the hot plate was cooling, the voltage of fiber optic sensor overshot as seen in figure 5.6.2. This was an unusual phenomenon. The thermistor showed to have a nice and steady descent. At the time, I broke an already broken sample to see if the glue was not cured properly. The glue was cured properly and was harden.

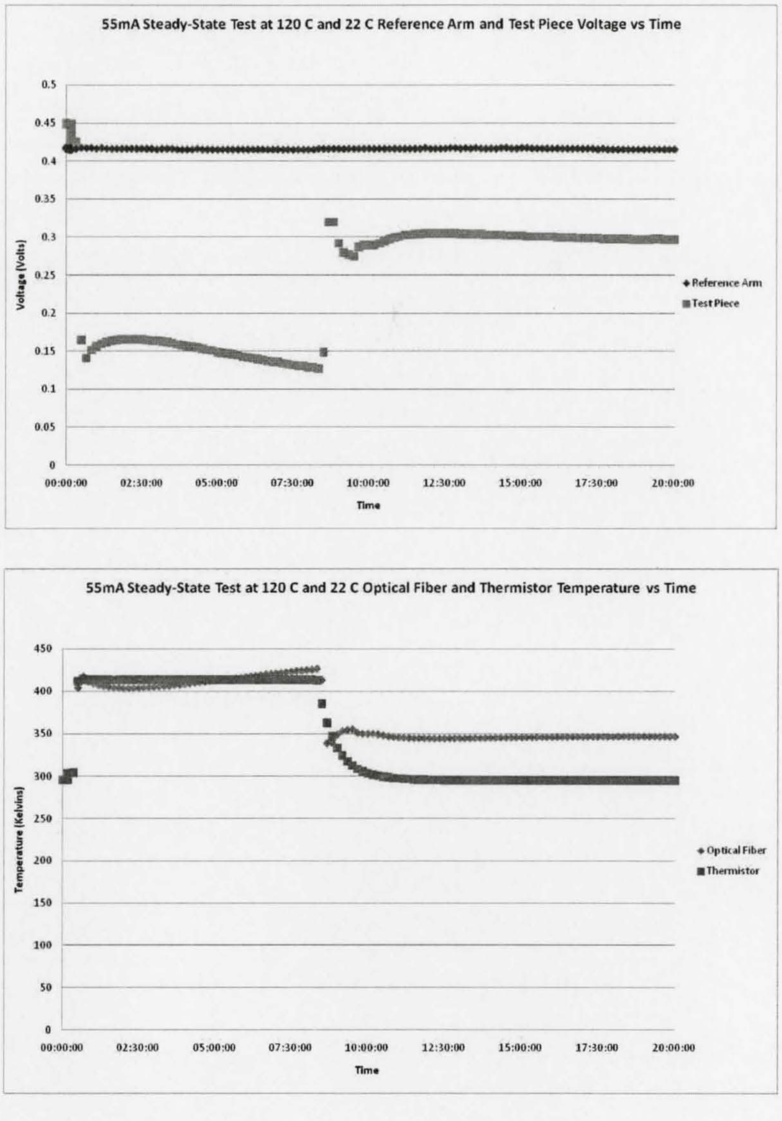
55mA Steady-State Test at 120 C and 22 C Reference Arm and Test Piece Voltage vs Time

55mA Steady-State Test at 120 C and 22 C Optical Fiber and Thermistor Temperature vs Time

Figure 5.6.3. Steady-State Test Taken On January 12, 2008

The equation for the voltage-temperature conversion had changed to the following:

$$\text{RelativeTransmission} = A''\cdot\exp\left(-KL\left(\frac{1.24}{\lambda}-1\ 1655+\frac{0.000473T^{2}}{T+\beta}\right)^{\frac{3}{2}}\right) \tag{5.2}$$

$$A''=\frac{A}{TransmissionAt295K}$$

In equation 5.2, the relative transmission was adjusted such that the equation is normalized to 22^{0}C. The reason was to match the constant with the thermal electric cooling temperature in the laser The 'A' value remained the same from the previous equation. The optical temperature curve fitted much better at higher temperatures than the previous two tests. Despite of the equation correction, this test was the most unusual case. The first part, the voltage from the optical temperature sensor varied from 120mV to 166mV throughout the eight-hour period. As the hot plate cooled, the voltage seemed to hit a maximum voltage of 305mV to 320mV Throughout the 22^{0}C steady-state, the voltage stayed between 305mV and 320mV After the experiment, I left the experiment alone for a few hours to see whether the voltage will rise back up, unfortunately it did not; as well, I cured it again. Thus I made a new starting voltage point at 315mV and ran a fourth test. This test, however, only took the 120^{0}C steady-state for two hours.

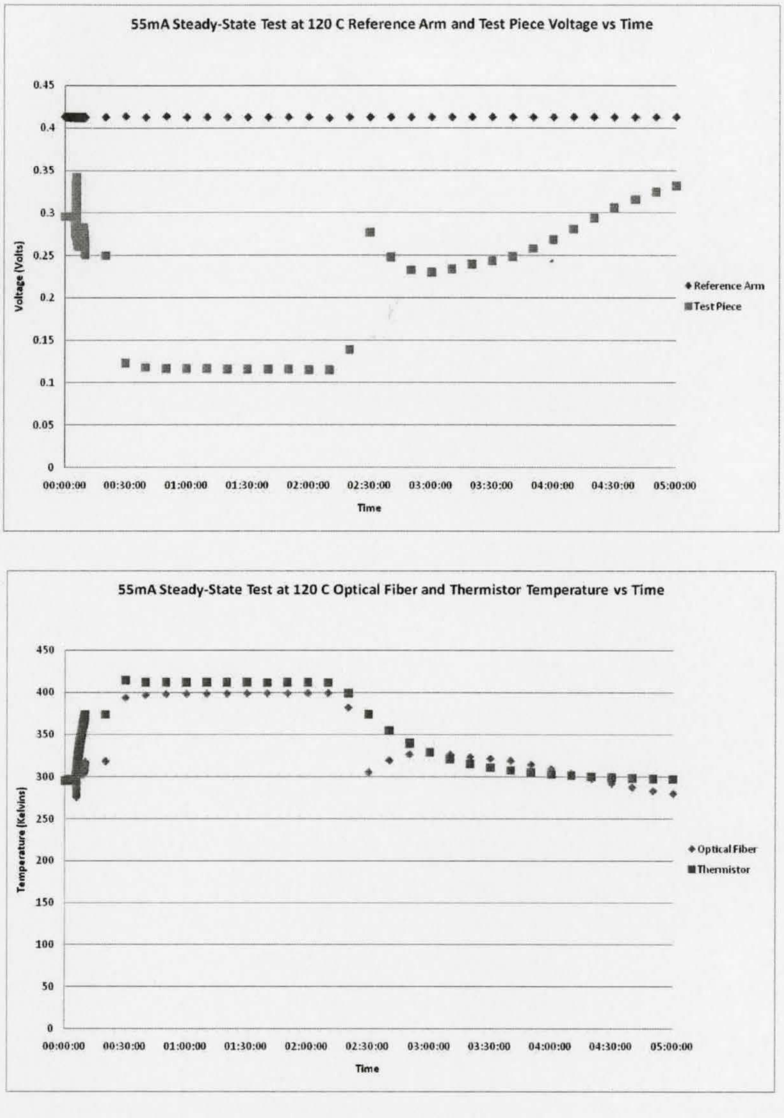

Figure 5.6.4. Steady-State Test Taken between January 12 and 13, 2008

Here in this test, the first ten minutes, the hot plate started to heat up and it gave some erratic behaviour, otherwise, at the steady state temperature, it was very accurate. As it cooled, the voltage spike appeared again. Thus, I did not know at all what is going on within the spike. The steady-state temperatures proved that the optical power detected from the optical fiber sensor did not drift. This is great for slow temperature change application. Unfortunately, the transient sections are not cohesive towards the hot-plate temperature.

5.7 Sawed Grooves Single-mode—Multimode on February 20, 2008

The new temperature device fabricated on February 20, 2008 is a single-mode—silicon—multimode temperature sensor This means that the input fiber to the device is single mode and the output fiber is multimode. This will prevent cladding modes in the fiber Instead of the doing a single ramp up and down temperature test, I did a cyclic temperature change from 35 degrees to 120 degrees Celsius. Three runs were performed on this single test.

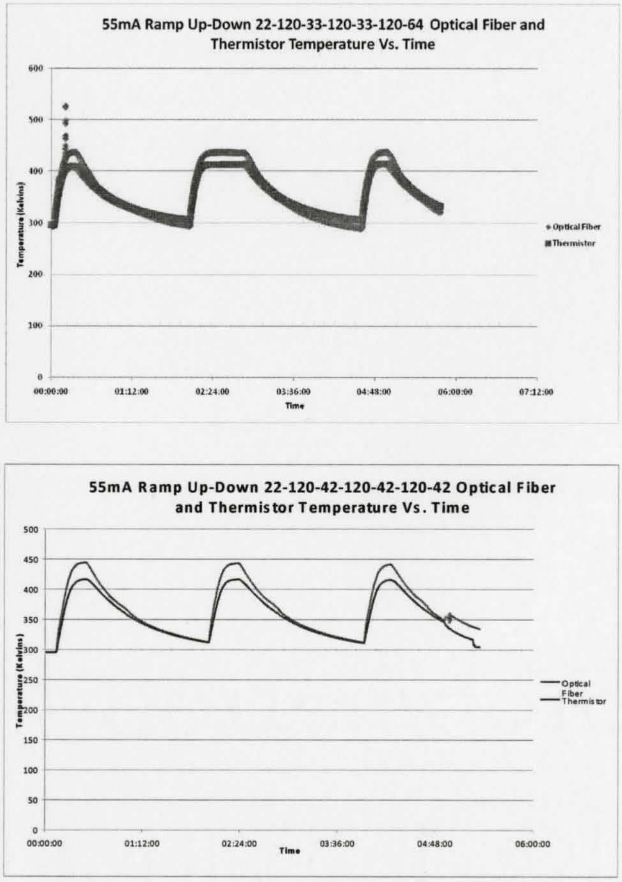

Figure 5.7 1 1st and 2nd Cyclic Test on a Single-mode-to-Multimode Sensor on February 20, 2008

The first rise in temperature in the first cyclic test had voltage drop. After, the fiber-optic sensor tracked the thermocouple reading very well. The remaining issue was to adjust the K and A value for the transmission-temperature calibration. With the second cyclic test, the ramp up-down cycles worked fine. The last cycle cooling down I shook the multi-mode fiber to see if it would not obscure the results. Unfortunately it did. Thus, using multimode fiber is not recommended.

5.8 1550nm Temperature Rise and Fall on February 25, 2008

On February 25, 2008 experiment, a double cycled test was performed on the SM-SM device built on February 15, 2008. In this experiment, the laser wavelength was changed to 1550nm. At this wavelength, the transmission of bulk silicon is nearly independent of temperature. The temperature dependence of the overall transmission depends on alignment and interference effect. Ideally with this setup, the signal should stay flat because the wavelength is far from the band-edge and in transmission will not change due to temperature. However, in reality, the signal is highly temperature dependent as shown in figure 5.8.1

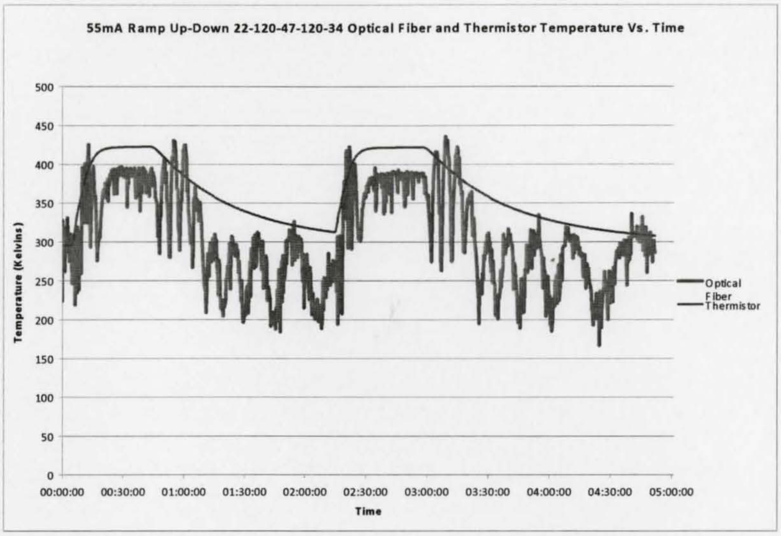

Figure 5.8.1 Cyclic Temperature Rise and Fall using 1550nm Laser on February 25, 2008

When I left the heater on for about 10 minutes at 120 Celsius, the signal settle with some deep noise, only voltage rises and not drops. I did a dual cycle and the pattern repeated itself nearly in sequence. This means that there are some alignment issues within the fiber connection.

Figure 5.8.1 also allows us to study the Fabry-Pérot effect of the sensor The silicon piece is the etalon of the effect. From equation 2.49 in the Fabry-Pérot section 2.3.4:

$$\frac{dm}{dT} = \frac{2l}{\lambda}\frac{dn}{dT} \qquad (2.49)$$

The rate of fringes per temperature is calculated to be 0.07897 fringe/^{0}C at 1550nm wavelength. Over the span of 120 degrees Kelvins, there should be 9.47 fringes; rounding it down to 9, we do have 9 fringes shown in figure 5.8.1.

5.9 Pre-Fabricated V-Grooves Temperature Experiment on March 20 to 22, 2008

After several experiments with unsatisfactory results, I concluded that there is fiber misalignment being caused by thermal material expansion throughout the device. The material expansion is very small; however, it does cause some problems. When I pushed down on the glue of the test piece, where the fiber is, the power output fluctuated. Thus, there is reason to believe that the sawed grooves were not the best choice. I bought several Si V-Grooves to see if they improved the alignment stability:

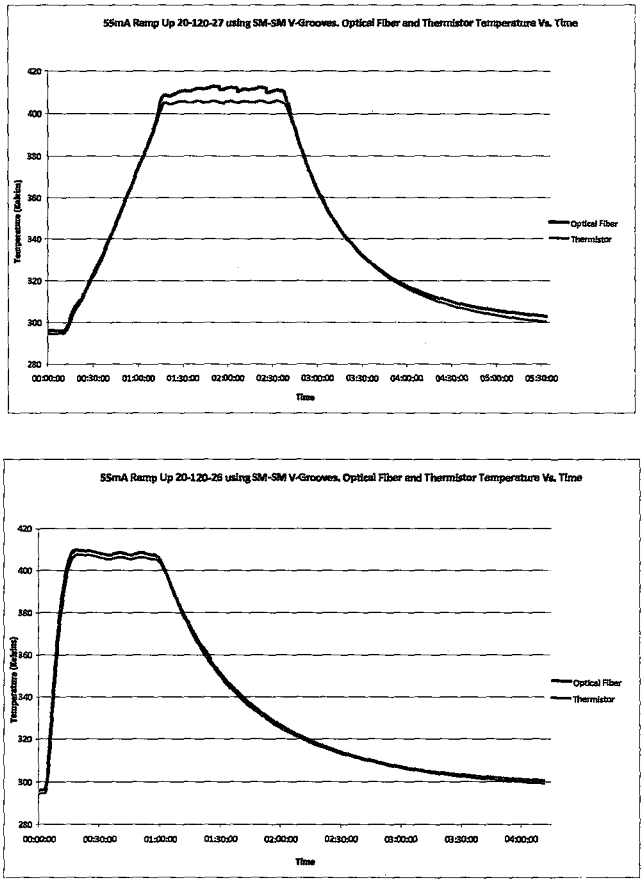

Figure 5.9.1: Two Temperature Tests Ran on March 21st and 22nd Respectively.

The first test was a slow heating process to see if there any abnormalities, mainly inconsistencies in the rate of change of voltage due to temperature. The hot plate heated the sensor at 100^{0}C per hour, then held steady for about an hour then does a full cooling. The second test had the heating rate of 400^{0}C per hour, held steady for an hour then does a full cooling. The new K value for this experiment in equation 5.2 was 3275. Both these tests show that the optical fiber sensor follows very well with the thermistor, within 2%. For the first test, there was a higher temperature reading in the optical fiber than the thermistor. This was due to the optical fiber sensor being very close to the hot plate and well insulated. The thermistor, on the other hand, was a bit off from the hot plate, thus showed the discrepancy.

5.10 Packaged Temperature Sensor Experiment on the motor on August 14, 2008

After fabricating and packaging a new temperature sensor head, it was placed onto the roughing pump motor in room A313 in the engineering building. The program was recording the data every second for one minute and forty seconds. After, the data was recording every five minutes up to forty hours. The purpose was to see how reliable the repeatability of the sensor. The thermistor was not used in the experiment due to complications with the equipment.

The results were satisfactory in the sense that the sensor can repeat the results from the pump. No voltage drop was detected during the 40-hour test.

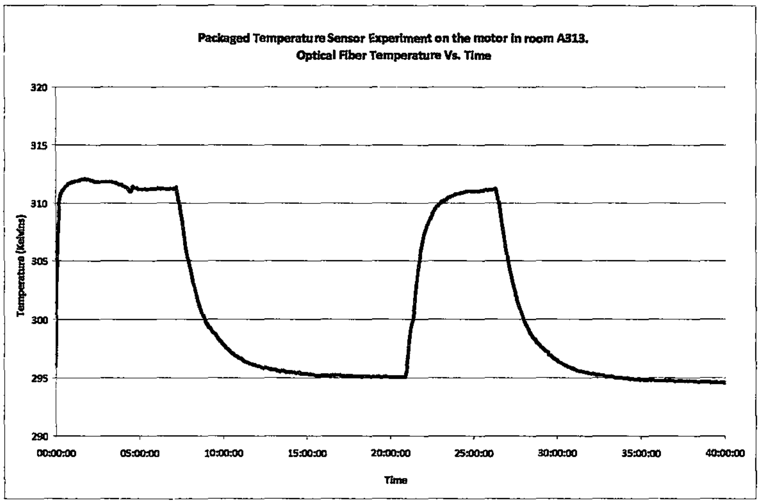

Figure 5.10.1: Packaged Temperature Sensor Experiment on the motor in room A313 performed on August 14, 2008. Motor was turned on at 1m40s and turned off at 7h11m40s. Then the motor turned back on at 20h56m40s and then turned off at 26h21m40s.

6 Vibration Sensor Results

6.1 Introduction

Like the temperature sensor, the data from the vibration sensor is recorded via LabView. However, the program is designed to present the data in the frequency domain. The frequency spectrum is calculated from the time-sampled raw data using Discrete Fourier Transform function, which is pre-built into the LabView program.

6.2 Modulation Test January 29, 2008

On January 29, 2008, I conducted an experiment to compare the signal in the time domain and the frequency domain. The laser used is a 1550nm diode laser from ILX Lightwave Technologies. The setup is two separate fibers on two different stages; one fiber is on a piezostage which was controlled by a piezocontroller; the other fiber was on a fixed stage. The experiment only lasted one second. The purpose of the experiment was to see how small of a modulation we can detect in the frequency domain even though we cannot see it in the time domain. I left out comparing the phases because I do not believe any viable information could come out of it.

What I have done to get the resolution for the 10Hz and 100Hz in the frequency range, I put the following settings for the 10Hz and 100Hz:

1. 10Hz modulation:
    a. Sampling Rate: 100Hz

    b. Number of Samples: 1000

    c. Total Time of Test: 10 Seconds

2. 100Hz modulation:

    a. Sampling Rate: 1000Hz

    b. Number of Samples: 1000

    c. Total Time of Test: 1 Second

The peak-to-peak voltage sent to the piezocontroller from a function generator is 500mV for both the 10Hz and 100Hz modulation. The 500mV peak-to-peak from the function generator translates to 3µm peak-to-peak on the piezostage.

The frequency response of the signal shows that there were spikes at 10Hz, 20Hz and 30Hz. After 30Hz, it was just noise and the overall magnitude drops. The time-domain graph shown in figure 6.2.1 shows the signal versus time of a single trace. The signal voltage is coming from the photodetector which the gain setting is at 0dB. The DC signal is 1.798V with the deviation of 705mV; thus the percentage of deviation for these results was 39.21%. Note that the two fibers were facing each other so the coupling power is 100%. In figure 2.3.3.5, the difference in coupling power is non-linear in respect of the radial offset.

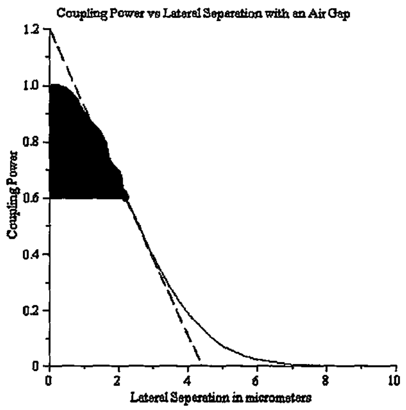

Figure 2.3.3.5: Figure 2.3.3.5: Coupling Power vs. Lateral Displacement with an Air Gap. The black area shows the range of the displacement.

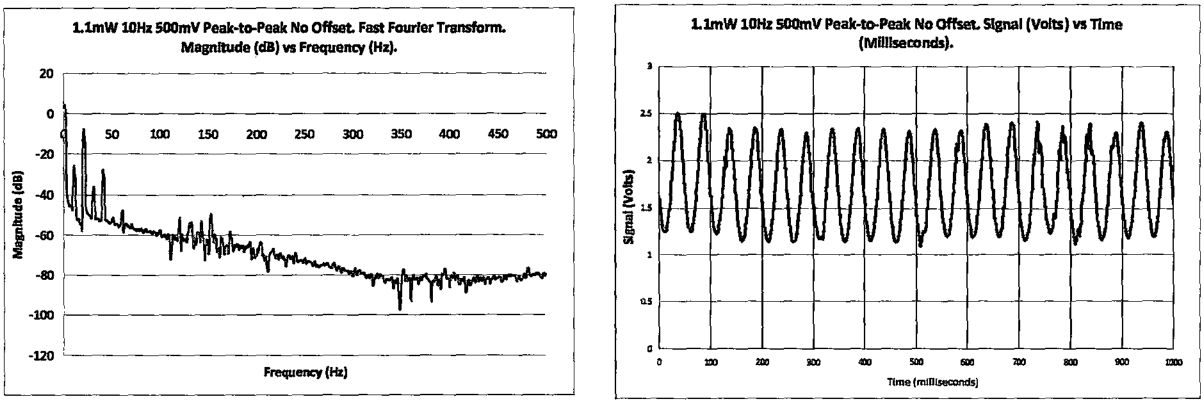

Figure 6.2.1: 1550nm laser 1.1mW 10Hz Modulation with a 500mVPP on the function generator, which is 3μmPP with the piezostage.

With the 100Hz modulation, the pattern repeated itself. Instead at the second cycle, the RMS voltage dropped from ~450ms and continues in an irregular pattern to ~950ms and then rises sharply again. In the frequency response, I see that there are spikes at 100Hz, 200Hz, 300Hz, 400Hz and a bit in the 500Hz range. The time-domain graph shown in figure 6.2.2 showed the signal versus time of a single trace. The signal voltage is coming from the photodetector which the gain setting is at 0dB. The DC signal was 1.344V with the deviation of 1.142V; thus the percentage of deviation for these results was 85%.

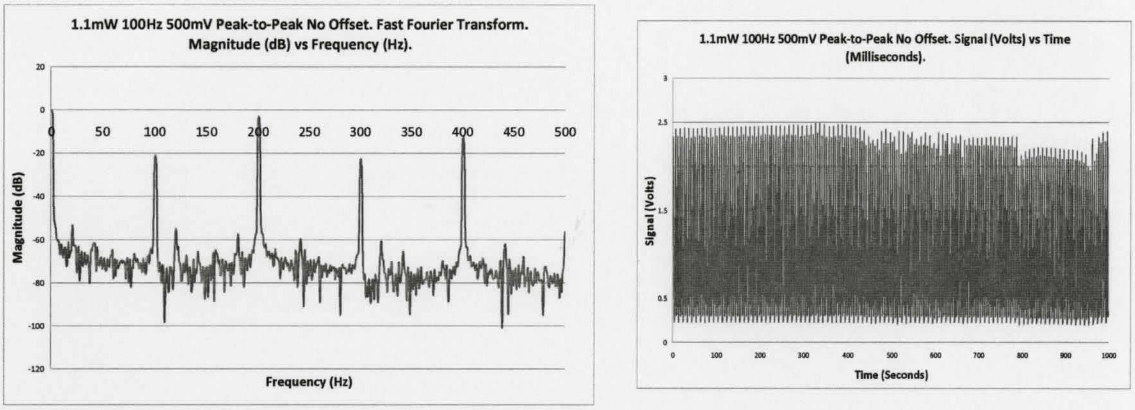

Figure 6.2.2 1550nm laser 1 1mW 100Hz Modulation with a 500mVPP on the function generator, which is 3μmPP with the piezostage.

6.3 Monotone Test on February 5, 2008

February 5, 2008 experiment consists of monotone and idle tests. The laser in use for this experiment is the 1550nm diode laser from ILX Lightwave 7900B. The monotone sound is a true sine wave from the speakers; thus isolating other wavelengths throughout the experiment. I only did the monotone at two frequencies: 0Hz and 293.66Hz. The 0Hz just represents the silence, or idle, testing. There were six tests in total and they all went in the following fashion:

1. 1.0dBm Laser Output. Input Short Tapered Fiber and Output 3.0mm Cantilever Hang SMF. 293.66Hz with Coherence Control On at 100Hz. Detector Gain at 60dB.
2. 1.0dBm Laser Output. Input Short Tapered Fiber and Output 3.0mm Cantilever Hang SMF. 0Hz with Coherence Control On at 100Hz. Detector Gain at 60dB.
3. 1.0dBm Laser Output. Input Short Tapered Fiber and Output 3.0mm Cantilever Hang SMF. 0Hz with Aluminum Foil Cover Detector Gain at 60dB.
4. 1.0dBm Laser Output. Input Short Tapered Fiber and Output 3.0mm Cantilever Hang SMF. 293.66Hz with Aluminum Foil Cover Detector Gain at 60dB.

5. 1.0dBm Laser Output. Input Short Tapered Fiber and Output 3.0mm Cantilever Hang SMF. 293.66Hz with Aluminum Foil Cover Speakers are facing the ground. Detector Gain at 60dB.
6. 10.0dBm Laser Output. Input Short Tapered Fiber and Output 3.0mm Cantilever Hang SMF. 293.66Hz with Aluminum Foil Cover Both SMF and Tapered Fiber are short to act as fixed ends. Speakers are facing the ground. Detector Gain at 60dB.

The fourth test with the 293.66Hz vibration will be analyze. Despite that the speakers were faced to the table, there were some significant vibration propagating on the table and in the air

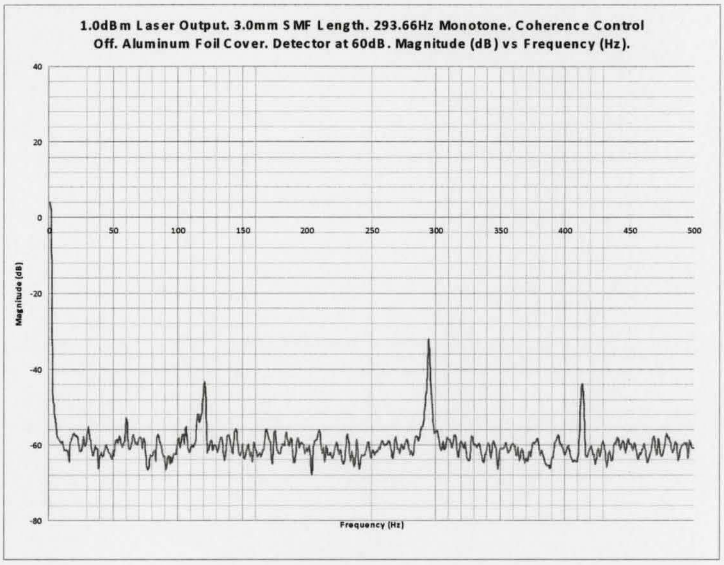

Figure 6.3.1 1 0dBm Laser Output. 3.0mm SMF Length. 293.66Hz Monotone. Coherence Control Off. Aluminum Foil Cover Detector at 60dB. Magnitude (dB) vs Frequency (Hz).

The 293.66Hz shows a lot of dominance throughout the frequency spectrum. However, there is a spike at 415Hz. This spike could just come from the single tone which made a fluke change in frequency. In conclusion, I have isolated the dominant frequencies in the frequency spectrum; thus I need to get the vibration sensor to a suitable platform to run further and controlled experiments. As far as the monotone detection goes, the sensor can pick up the monotone very easily.

6.4 Built Vibration Sensor Vibrating on the X and Z Axis March 6, 2008

March 6, 2008 experiment concentrates on the variation of amplitudes with the piezostage. The sensor has been built using the silicon platform and the length of the cantilever is 5mm long. I switched to the 1064nm laser from QPhotonics. The vibration will act on the X and Z axes independently.

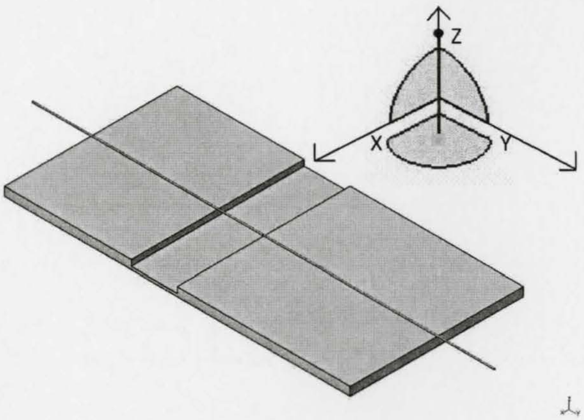

Figure 4.2.1 Drawing of the Vibration Sensor

There is a frequency at 60Hz due to the electrical pick-up and/or some residual AC line frequency in the laser output; this can be significant enough to block the frequency detection. LabView can detect vibration and can send an output as a single number; however, this will only work if the desire frequency has the higher magnitude in comparison to the 60Hz line frequency. The single number output can prove useful to find the overall acceleration of the apparatus. Below is the table of the various amplitudes, according to the function generator, and which axis the piezostage is vibrating:

- No Detection: The 60Hz frequency has a higher magnitude than the input frequency.

- Half Detection: Both the 60Hz frequency and the input frequency have the same magnitude but the program has a hard time detecting which one is which.
- Full Detection: The input frequency has the higher magnitude.

Amplitude (mVPP)	X-Axis	Z-Axis
100	No Detection	No Detection
200	No Detection	Full Detection
400	No Detection	Full Detection
800	Half Detection	Full Detection
1500	Full Detection	Full Detection

Table 6.4.1: The Detection Table in the X and Z Axis with respect to Amplitude

The table above concludes that the device is more sensitive on the Z-Axis rather than on the X-Axis. This can work in the plant in Dofasco because the sensor will be place on top of the motor. The motor will be vibrating on the Z-Axis, depending on the placement of the sensor.

6.5 Shake Table Z-Axis Vibration Test on March 11, 2008

March 11, 2008 experiment consists of one test, the sensor on a shake table. The shake table vibrates at 100Hz at 1g or $9.81m/s^2$ RMS.

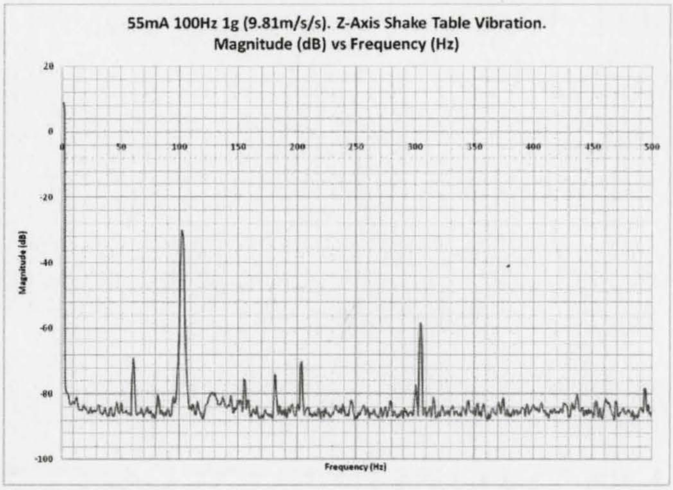

Figure 6.5.1 Frequency Response Results of the Shake Table.

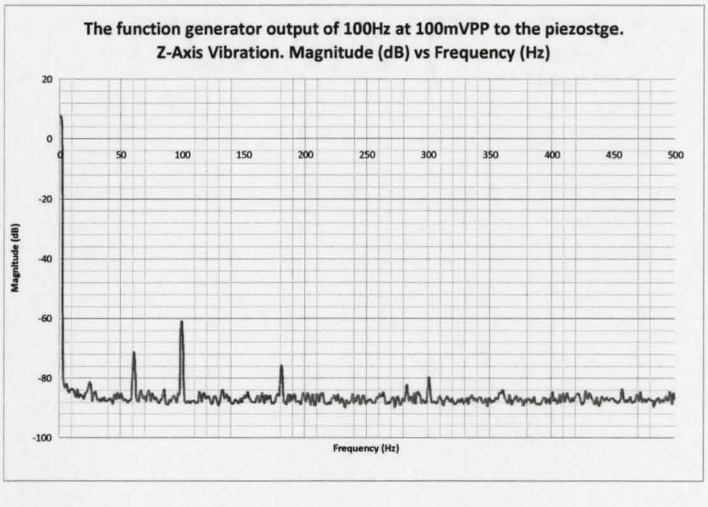

Figure 6.5.2. Frequency Response Results from the Piezostage with the Function Generator

The observed vibration frequency spectrum shown in figure 6.5.1, a dominant frequency at 100Hz is seen. There are frequencies at 60Hz, 200Hz and 300Hz, but that is the nature of the device vibrating. At 1g, the device can read the acceleration quite well; a 60dB difference between the floor and the 100Hz's peak.

According to the distributed load calculations, the resonance frequency of the cantilever bar is 1967Hz at 5mm length. To have an accurate accelerometer, the input frequency must be lower than 25% of the resonance frequency The feature seen in the graphs shown in figure 6.5.1 and 6.5.2 are well below this limit. When we compare it to a previous Z-Axis vibration test, the difference between the 100Hz magnitude and the floor is only 25dB.

6.6 Optical Chopper Motor Test on April 9, 2008

In the April 9, 2008 experiment, the vibration sensor was subjected to vibration from an optical chopper motor I built another vibration sensor but with a 4mm cantilever beam. The optical chopper is a DC motor that drives a disc with many holes. The optical chopper was a convenient motor that could simulate a real DC motor in the factory. The disc of the optical chopper should provide some imbalance in the motor, causing it to vibrate; however, the disc is perfectly balanced but the stand is not; thus there was some vibration. The optical chopper RPM, frequency in this case, is controlled by the motor control provided. The input frequencies shown are the actual input frequencies of the motor

Figure 6.6.1 Diagram of the Optical Chopper Setup

With the setup shown above, the experiment consists of two simple tests:

1. 83.33Hz Motor Rotation Speed (MRS), 2 000Hz Sampling Rate at 2 000 Samples per Cycle
2. 83.33Hz Motor Rotation Speed, 10 000Hz Sampling Rate at 10 000 Samples per Cycle

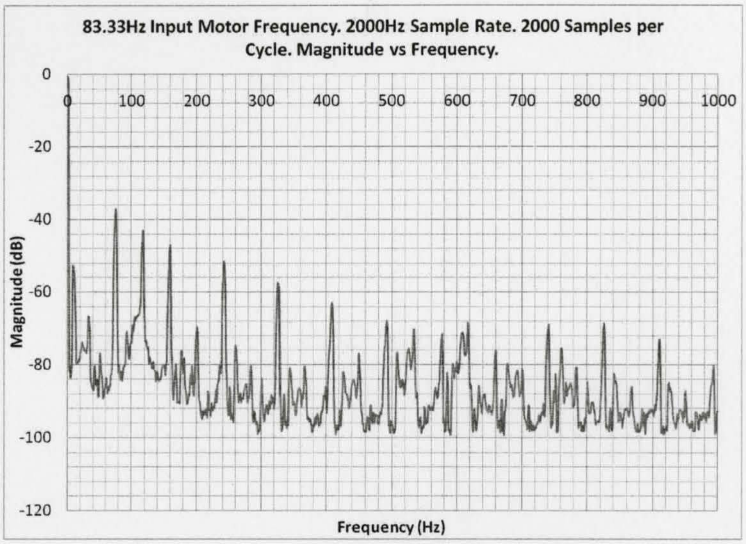

Figure 6.6.2. 83.33Hz MRS, 2 000Hz Sampling Rate at 2 000 Samples per Cycle

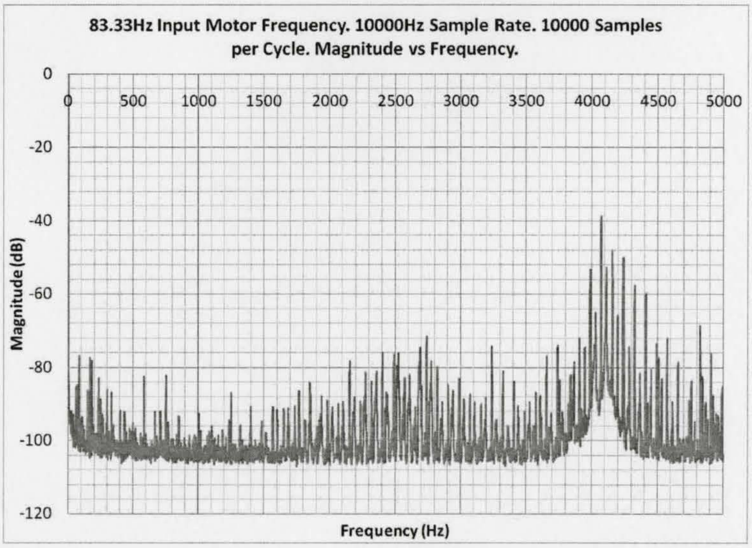

Figure 6.6.3. 83.33Hz MRS, 10 000Hz Sampling Rate at 10 000 Samples per Cycle

Around 4000Hz, there is a jump in magnitude; this is where the resonance frequency of the motor. To have a good sensor, the sample frequency must be less than 1250Hz.

6.7 5mm Cantilever Sensor Piezostage and Optical Chopper on April 21, 2008

I constructed a new vibration sensor that has a 5mm cantilever beam, in order to increase the sensitivity. I then conducted two separate experiments: piezostage vibration and the optical chopper motor vibration. The piezostage vibration experiments consist of four tests, all at 100Hz:

1. X-Axis at 800mVPP Amplitude. 1000Hz Sampling Rate, 1000 Samples per Cycle.
2. Z-Axis at 800mVPP Amplitude. 1000Hz Sampling Rate, 1000 Samples per Cycle.
3. Z-Axis at 1600mVPP Amplitude. 1000Hz Sampling Rate, 1000 Samples per Cycle.
4. Z-Axis at 1600mVPP Amplitude. 10 kHz Sampling Rate, 10k Samples per Cycle.

I compare the 5mm results taken on April 21, 2008 from the 4mm results taken on April 7, 2008. From there, I concluded that the sensitivity of the 5mm cantilever on the Z-Axis at 100Hz, 800mVPP amplitude is higher than the 4 mm, by 10dB. However, on the X-Axis, it seems that the 4mm cantilever beam is more sensitive than the 5mm by 7dB, which is very unusual.

With the optical chopper, I tested the sensor at different motor speeds. The motor speeds will represent the input frequency. The vibration of the motor may not coincide with the frequencies. The optical chopper has an off-centered mass to cause an imbalance in the structure. This will allow a larger induced vibration throughout the structure. Below are the three groups of tests we have done with the optical chopper.

1. 33.33Hz MRS both reading at 1000Hz and 10 kHz sampling rate.
2. 55.50Hz MRS both reading at 1000Hz and 10 kHz sampling rate.
3. 66.67Hz MRS both reading at 1000Hz and 10 kHz sampling rate.

In addition to taking the frequency spectrum of the tests, I took the raw signal data to see the waveform in the time domain.

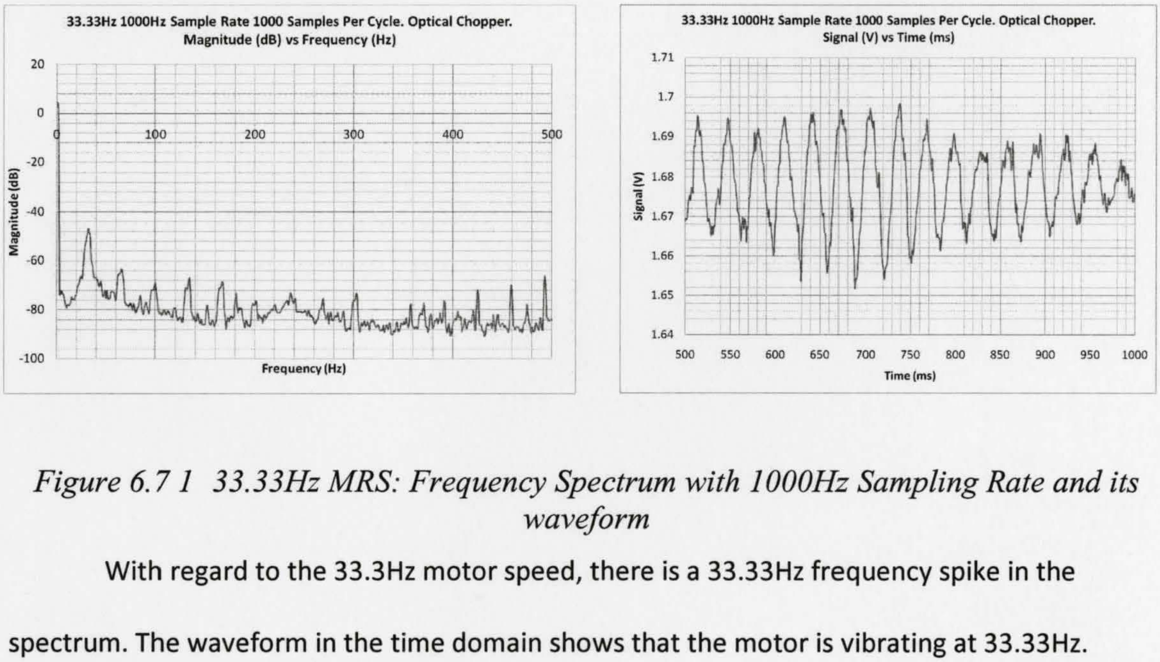

Figure 6.7 1 33.33Hz MRS: Frequency Spectrum with 1000Hz Sampling Rate and its waveform

With regard to the 33.3Hz motor speed, there is a 33.33Hz frequency spike in the spectrum. The waveform in the time domain shows that the motor is vibrating at 33.33Hz.

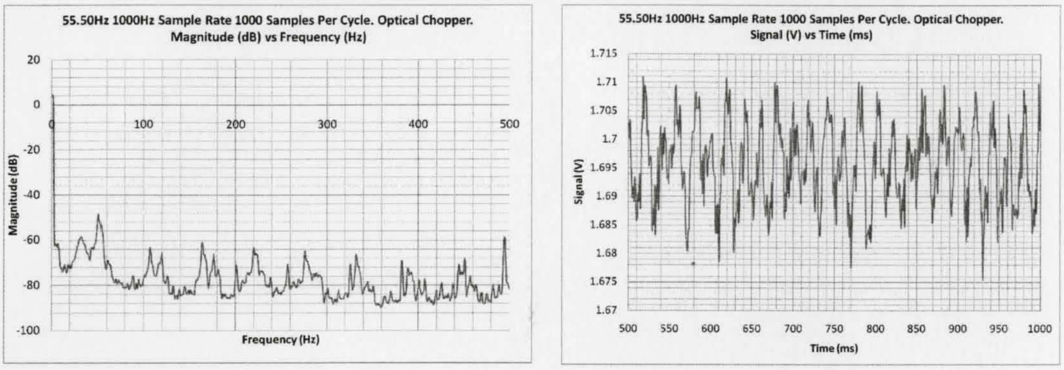

Figure 6.7.2 55.50Hz MRS: Frequency Spectrum with 1000Hz Sampling Rate and its waveform

Same ordeal with the 55.50Hz, the vibration sensor picks up the motor speed. The waveform is verifies the motor speed in the frequency spectrum.

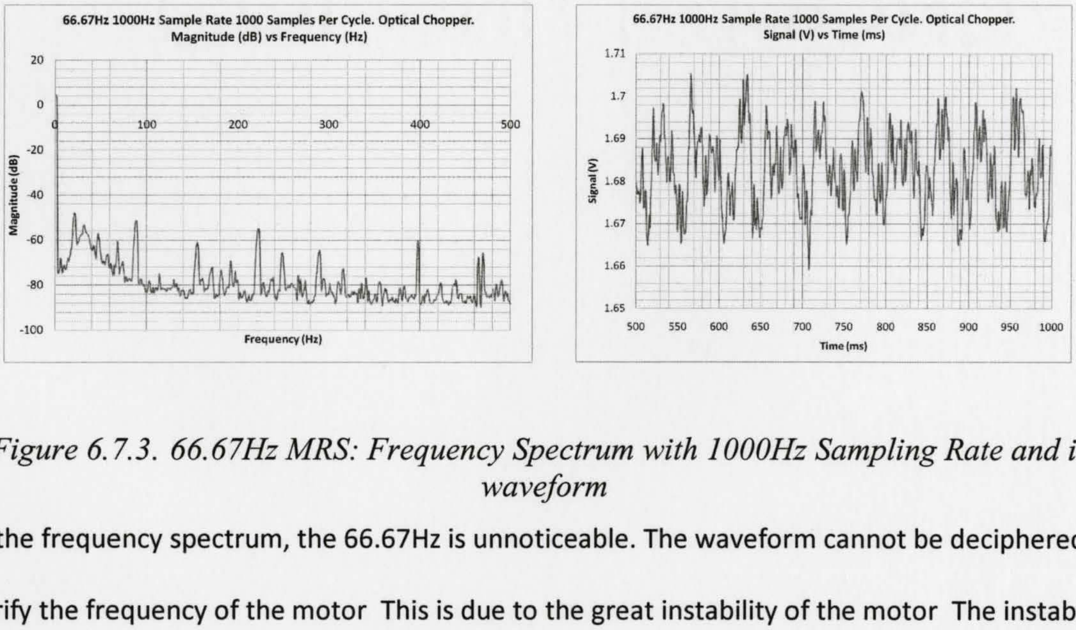

Figure 6.7.3. 66.67Hz MRS: Frequency Spectrum with 1000Hz Sampling Rate and its waveform

In the frequency spectrum, the 66.67Hz is unnoticeable. The waveform cannot be deciphered to verify the frequency of the motor This is due to the great instability of the motor The instability will skew the results, and the program would have a hard time to decipher the frequency of the motor

7 Dofasco Field Tests

The Dofasco field tests were a series of tests taken in different sections of the plant. The purpose of the field tests was to see the performance level of the vibration sensor My vibration sensor has a sensitivity of 0.00866 V/m for the calibration of the acceleration reading. The length of the fiber optic cantilever is 4mm, which the resonance frequency is 5019Hz. In the lab, the original sensitivity of the sensor, unpackaged, was 0.00838 V/m.

The testing is split into two phases. The first phase consists of tests inside the power house. The configuration of the powerhouse is shown below:

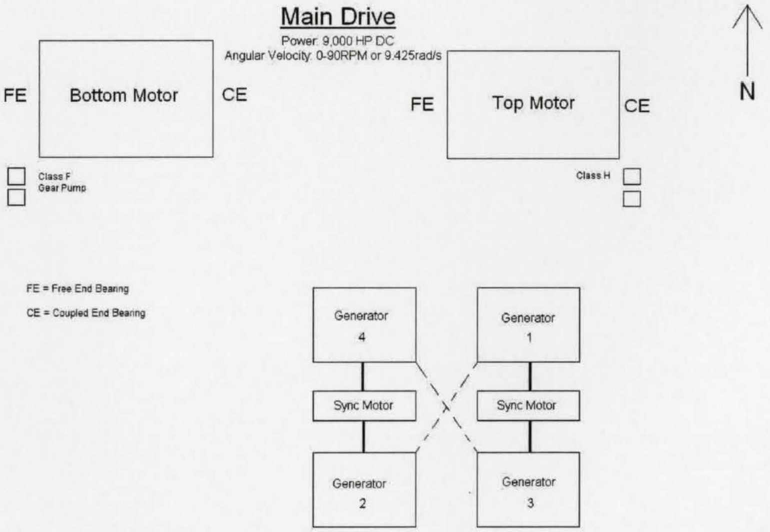

Figure 7 1 Top View of Power House

I expect the results from the power house to contain the 60Hz line frequency due to the motors' electrical components.

The second phase consists of tests inside the water pump house. The configuration of the water pump house is shown below:

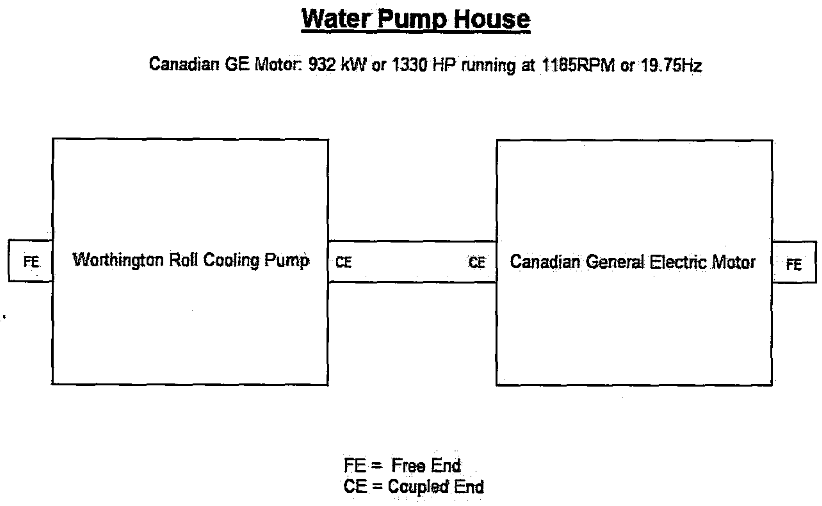

Figure 7.2: Top View of Water Pump House

For the cooling pump, I do not expect a 60Hz line frequency since there is no dominating electrical components inside; however, there should be a 60Hz line frequency in the motor due to its electrical components.

During the phases, there was a plethora of data recorded and extensive amount of graphs plotted; however, only a selected few graphs will be shown and explained upon the importance of the sensor's performance: comparison towards the other two sensors and any mechanical relevance that must be pointed out.

7.1 Top and Bottom Motor Free End Bearing Comparison

The purpose of comparing the top and bottom motors' free end bearings was to see what the common frequencies are and observe the performance of the vibration sensor. Note that the 60Hz and its apparent harmonics must be ignored because they are the line frequencies. The sampling rate and number samples for the two are 1000Hz and 1000 samples per cycle. The discussion will be based on the measurements taken on the horizontal radial direction (X-direction).

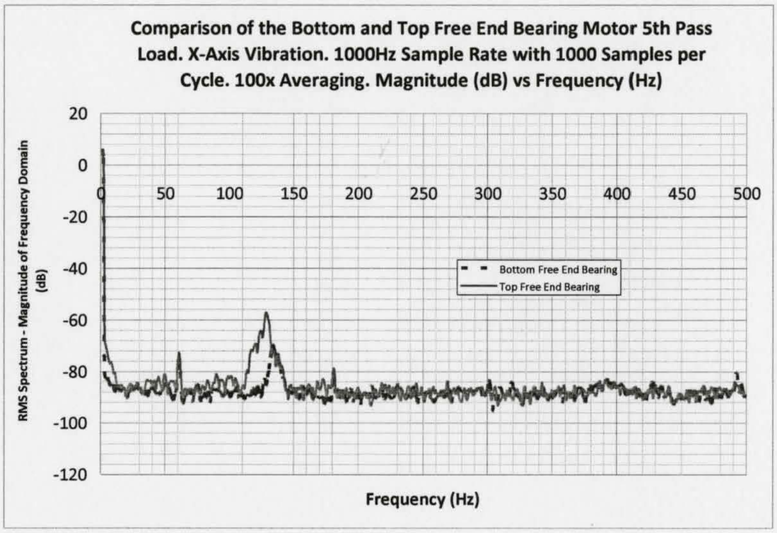

Figure 7 1 1 Bottom and Top Motor's Free End Bearings Results. 1000Hz Sampling Rate, 1000 Samples per Cycle. X-Axis measurement.

The noticeable issue in this comparison is the frequency at 130Hz. The bottom's free end bearing's frequency is sharper than the top's. To measure the sharpness, the Q factor must be implemented:

$$Q = \frac{f_0}{\Delta f} \qquad (7\ 1)$$

The Δf is measured from half of the maximum power or 3dB. Thus for the bottom's Q factor, it is 44.667 while the top's Q factor is 25.8. These are approximate values; however the Q factor shows the frequency variance in these free end bearings.

7.2 Worthington Pump Coupled Bearing

During the vibration test of the Worthington pump coupled bearing, there are two issues that are important: the common frequency and aliasing. The common frequency issue is when I take the vibration readings at different sampling rates and samples, and see if there are similar frequency spikes that show up in the frequency spectrum. I used the following three sampling rates and samples:

1. 400Hz sampling rate, 1000 samples per cycle
2. 1000Hz sampling rate, 1000 samples per cycle
3. 4000Hz sampling rate, 4000 samples per cycle

With the three configurations, I have done the readings and plot the following graphs:

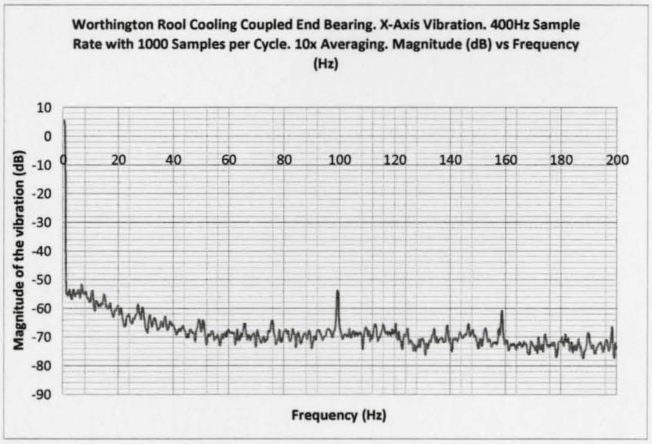

Figure 7.2.1 400Hz-1000SpC with the frequency spectrum of 0-200Hz.

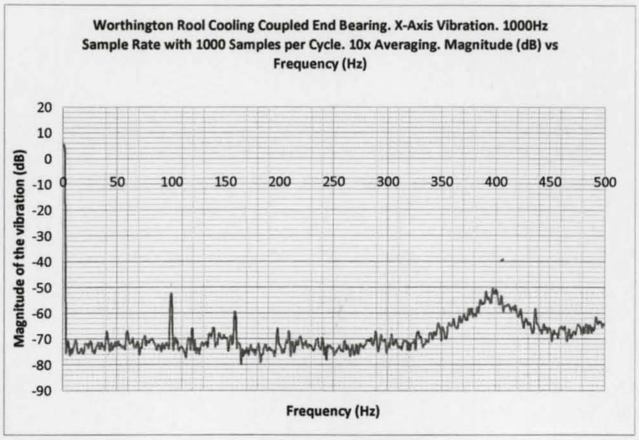

Figure 7.2.2 1000Hz-1000SpC with the frequency spectrum of 0-500Hz

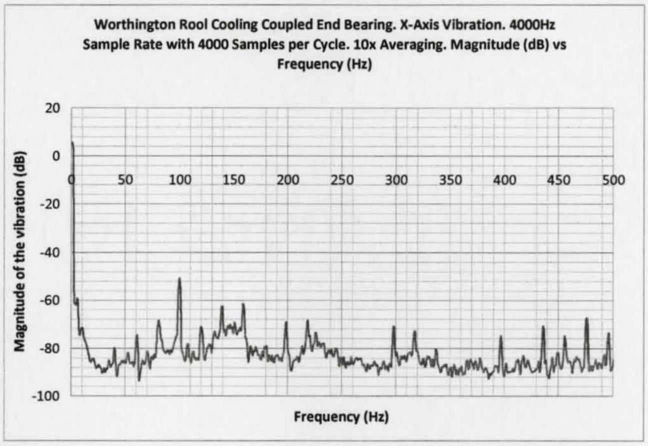

Figure 7.2.3. 4000Hz-4000SpC with the frequency spectrum of 0-500Hz

The reason why I have only show 0-500Hz for the 4000Hz-4000SpC is to concentrate the region of interest. The 100Hz frequency is dominant throughout the three graphs; however, there is the second issue that must be addressed: aliasing.

In order to have an accurate reading of the vibration with the pump's coupled bearing, I must have a high sampling rate which would approach towards the true signal rather than digitizing the signal. Despite the aliasing issue, the 100Hz is still dominant throughout the low sampling rate through the relatively high sampling rate.

8 Conclusion

The theory behind the temperature and vibration sensor has been proven via experiments done within the 2007-2008 academic year. The use of silicon filter technique in the temperature sensor proves that this simple technique can be used in the measurement of temperature. The use of the cantilever beam techniques proves that classic mechanics fused with optical engineering can produce a simple and effective vibration sensor.

The experimental results from the temperature sensor show some inconsistencies and faults. These results, specifically in section 5.6, were the result from faulty fabrication of the temperature sensor via sawed grooves. The sawed-grooves cause the fiber to shift around during the fabrication process and during the testing stage. When I tested the single-mode-to-multimode temperature sensor, the sensor followed the thermistor very well comfortably. Unfortunately, multimode fibers distort the signal; thus, making it an undesirable choice. When I switched from the sawed-grooves to etched V-grooves, the temperature sensor behaves correctly. The reason is the fibers are fixed in the grooves such that the fibers will not shift.

The experimental results from the vibration sensor are satisfactory. Using different cantilever lengths (4mm and 5mm), the results show the expected difference in sensitivity. The longer the cantilever length, the more sensitive the sensor will be. However, the range of frequencies decreases. Therefore, I concluded that using a 4mm cantilever fiber is optimal in the vibration sensor. For the single-tone measurements, the vibration sensor reads them accurately and precisely. As for the motors' measurements, there were some aliasing issue. The aliasing came from the equipment itself since the data acquisition board (DAQ board) only supports up to

20kS/s. To go around this issue, I took measurements at different sampling rates and number of samples.

The Dofasco field tests show the versatility and the endurance of the packaged vibration sensor. Despite that it is a biaxial sensor, the measurements were acceptable from the Dofasco officials. The packaged sensor undergone eruptive shocks from the power house when the steel passes through, and it still survived. More importantly, the sensor still functions correctly. Another issue that could have been analyzed is the fatigue limit of the cantilever fiber. However, it is more of a mechanical/material engineering issue rather than an optical engineering issue and was not discussed in this thesis.

Overall, the temperature and vibration sensors show success. They were tested in harsh environments and they functioned correctly. In the future, these sensors could be mass produced inexpensively for the hot mill at Dofasco. Therefore, there is promise for these temperature and vibration sensors.

Appendix A: Mechanics Derivations

Equation 2.8/2.9 Derivation

$$\frac{d\vec{r}}{dt}|_I = \frac{d\vec{r}}{dt}|_B + \vec{\omega} \times \vec{r} \qquad (2.8)$$

$$\vec{v} = \dot{\vec{r}} + \vec{\omega} \times \vec{r}$$

$$\frac{d\vec{v}}{dt}|_I = \frac{d\vec{v}}{dt}|_B + \vec{\omega} \times \vec{v}$$

$$\frac{d\vec{v}}{dt}|_I = \frac{d(\dot{\vec{r}} + \vec{\omega} \times \vec{r})}{dt}|_B + \vec{\omega} \times (\dot{\vec{r}} + \vec{\omega} \times \vec{r})$$

$$\frac{d\vec{v}}{dt}|_I = \ddot{\vec{r}} + \dot{\vec{\omega}} \times \vec{r} + \vec{\omega} \times \dot{\vec{r}} + \vec{\omega} \times \dot{\vec{r}} + \vec{\omega} \times \vec{\omega} \times \vec{r}$$

$$a = \ddot{\vec{r}} + \dot{\vec{\omega}} \times \vec{r} + 2\vec{\omega} \times \dot{\vec{r}} + \vec{\omega} \times \vec{\omega} \times \vec{r} \qquad (2.9)$$

Equation 2.12 Derivation

$$q = -w$$

$$EI\frac{d^3y}{dx^3} = -wx + C_1$$

$$EI\frac{d^2y}{dx^2} = \frac{-wx^2}{2} + C_1x + C_2$$

$$EI\frac{dy}{dx} = \frac{-wx^3}{6} + \frac{C_1x^2}{2} + C_2x + C_3$$

$$EIy = \frac{-wx^4}{24} + \frac{C_1x^3}{6} + \frac{C_2x^2}{2} + C_3x + C_4$$

$$EI\left.\frac{d^3y}{dx^3}\right|_{x=L} = 0 \rightarrow C_1 = wL$$

$$EI\left.\frac{d^2y}{dx^2}\right|_{x=L} = 0 = \frac{-wL^2}{2} + wL^2 + C_2$$

$$C_2 = -\frac{wL^2}{2}$$

$$EI\left.\frac{dy}{dx}\right|_{x=0} = 0 = C_3$$

$$EIy(0) = 0 = C_4$$

$$EIy(0) = -\frac{wx^4}{24} + \frac{wLx^3}{6} - \frac{wL^2x^2}{4} \qquad (2.12)$$

Appendix B: Index

Appendix C: References

1. Hull, Robert, "Variation of Bandgap with Temperature in c-Si," Properties of Crystalline Silicon, INSPEC The Institute of Electrical Engineers, 1999, 391: *Article is written by J. Weber in October 1997*
2. Hull, 392
3. Goksen, K. et al., "Dispersive optical constants and temperature tuned band gap energy of Tl_2InGaS_4 layered crystals," Journal of Physics: Condensed Matter 19 (2007) 256210 (8pp), 5 June 2007, 5, http://www.iop.org/EJ/article/0953-8984/19/25/256210/cm7_25_256210.pdf
4. Callister Jr, William D., "22.7 Absorption," Materials Science and Engineering: An Introduction, John Wiley & Sons, Inc., 1997, 702
5. Yang, Edward S., "Semiconductor Fundamentals," Fundamental of Semiconductor Devices, McGraw-Hill, 1978, 20-21
6. Anonymous, "Basic Parameters for Zinc Blende crystal structure," BN – Boron Nitride, n.d., n.p., http://www.ioffe.ru/SVA/NSM/Semicond/BN/basic.html
7. Rodrigues, Luis Filipe Raposo, "Chapter 2: Vehicle Model and Problem Definition," Hybrid Control of an Underactuated Underwater Shuttle for the Deployment of Benthic Laboratories, Universidade Técnica de Lisboa, Instituto Superior Técnino, 15 September 1997, 30-31

8. Norton, Robert L., "4.10 Deflection in Beams," Machine Design, Prentice-Hall Inc., 2000, 168-170
9. Norton, "3.3 Load Analysis," 78-81
10. Norton, "3.9 Beam Loading," 116-120
11. Norton, "3.7 Vibration Loading," 106-110
12. Norton, "4.14 Spring Rates," 192-193
13. Lee, Donald L., "Introduction," Electromagnetic Principles of Integrated Optics, John Wiley & Sons, Inc., 1986, 1-2
14. Lee, "Basic Electromagnetic Theory: 2.5 Phase Velocity," 24-25
15. Pedrotti, S.J., Frank L. and L. S. Pedrotti, "Production and Measurement of Light," Introduction to Optics, Prentice-Hall, Inc., 1987, 8
16. Pedrotti, "Nature of Light," 5
17. Pedrotti, "Nature of Light," 3
18. Pedrotti, "Physical Constants," xxiv
19. Johnson, Sergio, "Bessel Beam Theory," "Nondiffracting" Light Beam, College of Optical Sciences, University of Arizona, n.d., 3, http://www.u.arizona.edu/~sergioj/draft1.doc
20. Ramachandran, Siddharth, "FIBERS FOR FIBER LASERS: Higher-order mode propagation may enable power scaling," LaserFocusWorld, 1 May 2007, n.p., http://www.laserfocusworld.com/articles/292403
21. Lee, "Basic Electromagnetic Theory: 2.1 Maxwell's Equations," 13

22. Lee, "Basic Electromagnetic Theory: 2.4 The Wave Equation in Source-Free Isotropic Media," 18-21

23. Rüdiger, Dr. Paschotta, "Gaussian Beams," Encyclopedia of Laser Physics and Technology, RP-Photonics Consulting GmbH, 27 March 2008, n.p., http://www.rp-photonics.com/gaussian_beams.html

24. Optics for Research, Fiber-Optic Products, Optics for Research Inc., 2001, 1, http://www.ofr.com/misc/OFR_2001_Fiber.pdf

25. Moore, Lori, Single Mode Fiber Coupling: Sensitivity and Tolerancing, University of Arizona, 6 December 2006, 9, http://www.optics.arizona.edu/optomech/Fall06/work/521/Tutorials/LMooreTutorial1.doc

26. Pedrotti, "Fringe Profiles – The Airy Function," 293

27. Pedrotti, "External and Internal Reflections," 479

28. Meyer-Arendt, Jurgen R., M.D., "Thin Films", Introduction to Classical and Modern Optics, Prentice-Hall, Inc., 1984, 260

29. Meyer-Arendt, 262

30. Beckwith, Thomas G., Roy D. Marangoni and John H. Lienhard V, "4.5 Frequency Spectrum," Mechanical Measurements, Addison-Wesley Publishing Company, 1993, 142

31. Beckwith, "4.6.1 The Discrete Fourier Transform," 145

32. Weimer, Melissa Ray, Waveform Analysis Using The Fourier Transform, DATAQ Instruments, Inc., 2008, n.p., http://www.dataq.com/applicat/articles/an11.htm

33. Beckwith, "4.6.2 Frequencies in Discretely Sampled Signals: Aliasing and Frequency Resolution," 147

34. Beckwith, 150

35. Anonymous, "Sample Frequency," Aliasing, Wikipedia, Wikimedia Foundation Inc., n.d., n.p., http://en.wikipedia.org/wiki/Aliasing

36. Hunt, Kevin, Discussion of Aliasing Issue with the Vibration Sensor, 11 July 2008